doi:10.1038/nature12269

Contents

Bern3D-LPJ model description

The Bern3D-LPJ is an Earth System model of Intermediate Complexity (EMIC) with a fully coupled carbon cycle that consists of components representing the ocean and sea ice, ocean sediments, the atmosphere, and the terrestrial biosphere including peatlands and permafrost soils. Here we use a version that has recently been applied for experiments in the context of projects contributing to the Fifth Assessment Report of the IPCC (refs. 1–4). The ocean sediment component, however, was not included in the present study to reduce the computational cost and because sediment processes are largely insignificant on the time scales considered here.

The physical ocean model is based on the model by ref. 5 and described in detail by ref. 6. It is a global three-dimensional frictional geostrophic model with a horizontal resolution of 36×36 boxes and 32 vertical levels. Marine biogeochemistry and air-sea gas-exchange are implemented following OCMIP-2 (refs. 7, 8) with the extension of prognostic formulations for marine biological productivity as well as representations for the cycling of iron[9], silica[10], ^{13}C, and ^{14}C.

The atmosphere is represented by a two-dimensional energy and moisture balance model (EBM) as described by refs. 11, 12. Depth-integrated horizontal heat fluxes are parameterized in terms of eddy-diffusive fluxes with uniform zonal and latitude-dependent meridional diffusivities. Vertical shortwave radiation fluxes are calculated from incoming solar radiation[13], zonally averaged fractional cloud cover, and surface albedo[14]. The outgoing longwave radiation fluxes are parameterized after ref. 15 with additional radiative forcings due to CO_2 (ref. 16), other greenhouse gases, aerosols, and a feedback term, which is tuned to produce an equilibrium climate sensitivity of 3°C in the standard model setup.

The terrestrial biosphere component is an extended version of the Lund-Potsdam-Jena (LPJ) Dynamic Global Vegetation Model as used by refs. 17, 18, and described in detail by ref. 19. The model is run at a resolution of $3.75° \times 2.5°$ and represents vegetation by 12 plant functional types. The fertilization of plants by increasing atmospheric CO_2 concentrations is modeled according to the modified Farquhar scheme[20]. Potential damages and growth reduction by air-pollutants are not considered in the model. The LPJ version used here additionally includes a land use module[21,22], a new hydrology scheme[23,24] that allows for the simulation of permafrost dynamics and peatlands[24–26], and a land surface albedo component[27].

Parameter sampling

The 19 model parameters that are sampled in the Monte Carlo integration are given in Table S1. 11 parameters belong to the LPJ terrestrial biosphere model component and most of them are described in detail by ref. 19. The selection of these parameters was guided by the previous work of ref. 28. They analyzed an earlier version of the model by sampling 36 parameters and identified the most important ones in controlling carbon fluxes and pool sizes. α_a, α_{C3}, and θ control photosynthesis and g_m, the maximum canopy conductance, is an important hydrological parameter. Those four parameters were identified as the four most important ones for NPP and heterotrophic respiration and they are among the eight most important parameters controlling carbon pool sizes[28]. Further, τ_{sapwood} and $\mathrm{mort}_{\mathrm{max}}$ as well as f_{soil} and f_{slow} were selected because they belong to the most important parameters for vegetation and soil carbon pool sizes, respectively. In addition we chose three parameters that are likely to be important for the response of soil carbon under future warming. $\mathrm{resp}_{\mathrm{Q10,eq}}$ controls the temperature sensitivity of respiration and soil decomposition. This parameter is specified as a nominal Q_{10} temperature coefficient because this is commonly found in the literature. In fact the temperature sensitivity is modeled with an Arrhenius-type dependence[29] in which E_0 is modified as follows: $E_0 = 308.56 \cdot \frac{\log(\mathrm{resp}_{Q10,\mathrm{eq}})}{\log(2.4)}$. At moderate temperatures up to $\sim$20 °C the Arrhenius-type dependence corresponds approximately to the exponential dependence, at higher temperatures the sensitivity is lower for the Arrhenius-type dependence. $k_{\mathrm{soil,scale}}$ is a scaling factor applied to the decomposition rates of organic carbon in the fast and slow soil pools. Finally, $\mathrm{C}_{\mathrm{peat,scale}}$ determines the initial amount of carbon stored in northern peatlands.

Three parameters controlling the energy and moisture balance model of the atmosphere (EBM) are sampled. $\mathrm{diff}_{\mathrm{zonal}}$ and $\mathrm{diff}_{\mathrm{merid,scale}}$ control the depth-integrated heat fluxes in terms of zonal and meridional eddy-diffusive fluxes[11,12]. The uniform zonal diffusivity is specified directly and $\mathrm{diff}_{\mathrm{merid,scale}}$ is a scaling factor for the latitude-dependent meridional diffusivity. The third EBM parameter is the nominal equilibrium climate sensitivity. In the relatively complex model applied here the climate sensitivity cannot be specified explicitly. Instead the feedback parameter λ (refs. 11, 12) is adjusted according to a calibration curve to produce the specified equilibrium climate sensitivity. The effective climate sensitivity, however, corresponds only approximately to the nominal value because the calibration is done with the standard model setup and other parameters that are modified also influence the climate sensitivity.

Three parameters have been selected from the Bern3D ocean component. diff_{dia} and diff_{iso} are the diapycnal and isopycnal diffusivities that control the ocean circulation and thus the transport and vertical mixing of heat, carbon, and other tracers[6,30]. $k_{\text{gas,scale}}$ is a scaling factor applied to the OCMIP-2 air-sea gas transfer velocity field[31] and affects the oceanic uptake of anthropogenic carbon.

Finally, the last two parameters modulate the radiative forcing from well mixed greenhouse gases ($\text{RF}_{\text{GHG,scale}}$) and aerosols ($\text{RF}_{\text{aerosol,scale}}$). They are applied as scaling factors to the prescribed time series (or to the simulated RF in the case of CO_2) and reflect the uncertainties given by ref. 32.

We define a plausible range for each parameter based on literature and/or expert judgement (p_{min}, p_{max}; Table S1). Normal prior distributions (N) are chosen for ranges that are basically symmetric with respect to the standard parameter value (p_{std}) and log-normal priors (L) are used for asymmetric ranges:

$$N(x; p_{\text{std}}, \sigma) = \frac{1}{(\sqrt{2\pi}\sigma)} \exp(-\frac{(x - p_{\text{std}})^2}{2\sigma^2}), \quad (1)$$

$$L(x; p_{\text{std}}, s, l) = \frac{1}{(\sqrt{2\pi}s(x - l))} \exp(-\frac{(\ln(x - l) - \ln(p_{\text{std}} - l))^2}{2s^2}), \quad (2)$$

$$\sigma = \frac{p_{\text{max}} - p_{\text{min}}}{4}. \quad (3)$$

The shape (s) and location (l) parameters of the log-normal distributions are given in Table S1. They are chosen such that the median of the distribution matches p_{std} and the standard-deviation σ is $\frac{1}{4}$ of the parameter range, as for the normal distribution. This leads in most cases to distributions where the p_{min} to p_{max} range corresponds to the (largely symmetric) $\sim$95% confidence interval (c.i.). Exceptions are parameters where the considered parameter range is very asymmetric with respect to the standard value: g_m (69% c.i.; 29–98%), mort_{max} (83% c.i.; 15–98%), f_{slow} (63% c.i.; 35–98%), diff_{dia} (86% c.i.; 12–98%), and diff_{iso} (86% c.i.; 12–98%).

From the resulting prior distributions (Fig. S2) an ensemble of 5,000 model configurations is generated by sampling the parameter space by applying the Latin hypercube sampling method[33].

Observational constraints

The 26 observation-based data sets used to constrain the model ensemble are listed in Table S2. They range from single numbers to multi-dimensional gridded data sets in space and/or time. The data sets are organized in a hierarchical structure (Fig. S3) for aggregating the scores of individual constraints to the total score. This ensures both an adequate weighting of data sets with varying number of data points and also a balanced weighting between the different components of the carbon-cycle climate system.

For each ensemble member and each data set i, a relative mean squared error (MSE) is calculated as

$$\text{MSE}_i^{\text{rel}} = \sum_j a_j \frac{(X_j^{\text{mod}} - X_j^{\text{obs}})^2}{\sigma^2}. \tag{4}$$

X_j^{mod} and X_j^{obs} are the modeled and observed values at the data point j, respectively. a_j are the weights of the data points (i.e. volume or area for gridded data sets), and $\sigma^2 = \sigma^2_{\text{obs}} + \sigma^2_{\text{mod}}$ represents the combined observational error (σ^2_{obs}) and model discrepancy (σ^2_{mod}). While the observational error is given for most of the data sets, the model discrepancy is difficult to specify[34]. Following ref. 30 we estimate the combined error for each data set with the variance of the model-data difference for the best fitting model realisation (i.e. the model with the smallest MSE). In some few cases where the observational error is larger than this estimate (and thus the combined error is clearly underestimated), the observational error is taken as total error for logical reasons, i.e.

$$\sigma^2 = \max[\text{Var}(X^{\text{mod}} - X^{\text{obs}}), \sigma^2_{\text{obs}}]. \tag{5}$$

The $\text{MSE}_i^{\text{rel}}$ from individual targets are then aggregated by averaging over the group of variables at the same level in the hierarchical structure depicted in Fig. S3. From the World Ocean Atlas (WOA) temperature field, for example, first the $\mathrm{MSE}^{\mathrm{rel}}$ for the surface and the full three-dimensional fields are averaged. Then this average is combined with the results from S and PO_4 to get the average relative error for the group 'WOA', and so on. Finally, the mean $\mathrm{MSE}^{\mathrm{rel}}$ from the four main categories are averaged to get the total mean error. This gives the grouped land, ocean, CO_2 and heat constraints equal weights of $\frac{1}{4}$ with respect to the total score. This procedure can be summarized as $\mathrm{MSE}^{\mathrm{rel}}_{\mathrm{tot}} = \sum_i w_i \cdot \mathrm{MSE}^{\mathrm{rel}}_i$, where $w_i = \frac{1}{n_1} \cdot \frac{1}{n_2} \cdot \ldots$ is the product of weights at each level in the hierarchical structure given by the number of groups/data sets at the corresponding levels (e.g. $n_1 = 4$ for the main categories).

Finally the score $S_m = \exp(-\frac{1}{2}\mathrm{MSE}^{\mathrm{rel}}_{\mathrm{tot}})$ is calculated from the total average relative MSE for each ensemble member m and used as weight in all PDF calculations. S_m is a likelihood-type function and basically corresponds to a product of Gaussian distributions of data-model discrepancies with zero mean and variance σ^2. Yet the score S_m cannot be interpreted strictly in terms of likelihood since we do not account for the correlation structure of errors (i.e. autocorrelation of errors of a variable or correlations between different variables). As also noted by refs. 30, 35, 36 it is very challenging to extend full Bayesian calibration as described e.g. by ref. 34 to multivariate tracers and large data sets. To our knowledge, there currently exists no method to estimate error correlations in a computationally feasible way for such a large data set as used in this study. Nevertheless, the score S_m provides an indication of the relative performance of the models and can be used to constrain the ensemble.

To reduce computational cost, ensemble members with very low scores are discarded and not taken into account for the scenario simulations. The cumulative weight of the remaining 1,069 simulations is 99% of the total weight $\sum_m S_m$. Thus the difference in the posterior PDF of any variable obtained from the reduced ensemble is $\leq 1\%$ compared to the full 5,000-member ensemble.

Some data sets and model results had to be pre-processed for the MSE calculation. The gridded T, S, and PO_4 fields from the World Ocean Atlas 2009 (WOA09) were remapped to the model grid by volume-weighted averaging. The mapping error of the WOA09 data sets was estimated with the absolute difference between the analyzed and statistical mean fields. The total error (mapping error and standard error) was then remapped to the model grid and corrected with the square root of the number of aggregated grid cells. Similarly, the GLODAP data sets (alkalinity, CFC-11, dissolved inorganic carbon (DIC), and ^{14}C, including errors), soil carbon maps, and fAPAR fields were remapped to the model grid. No observational error is known for the soil carbon maps and the local NPP and vegetation-carbon estimates. In these cases σ^2 is given by the variance of the model-data difference for the best fitting model alone (Eq. 5).

To compare the annual atmospheric CO_2 cycle with local measurements at specific sites, the global atmospheric tracer model TM2 (ref. 37) was used to translate global fields of simulated monthly air-sea and air-land CO_2 fluxes to local concentration anomalies. Simulated monthly [CO_2] anomalies (mean 1950–2010) are then compared to the observed annual cycles at nine stations of the NOAA/ESRL cooperative air sampling network (GLOBALVIEW-CO_2; ref. 38). The nine stations are ALT (Alert, Nunavut, Canada, 82° N), BRW (Barrow, Alaska, USA, 71° N), AZR (Terceira Island, Azores, Portugal, 39° N), RPB (Ragged Point, Barbados, 13° N), CHR (Christmas Island, Republic of Kiribati, 2° N), ASC (Ascension Island, UK, 8° S), SMO (Tutuila, American Samoa, 14° S), AMS (Amsterdam Island, France, 38° S), and CGO (Cape Grim, Tasmania, Australia, 41° S).

Scenarios and model forcings

To explore the range of future anthropogenic greenhouse gas and aerosol emission trajectories, we use 55 scenarios that were provided by the integrated assessment modeling community. The set includes baseline ('business as usual') as well as mitigation scenarios that were generated with several Integrated Assessment Models (IAMs) which consider possible future demographic, economic, social, technological, and environmental developments. Four scenarios are the representative concentration pathways (RCPs) that have been selected for model experiments in preparation of the next IPCC assessment report[39,40]. 22 scenarios were developed as part of the Energy Modeling Forum Project 21 (EMF-21; refs. 41, 42), which served as a basis for the RCP selection. Further, we selected 6 out of the 20 scenarios provided by the

Greenhouse Gas Initiative (GGI; ref. 43) at IIASA and 23 out of the 64 scenarios from the Asia Modeling Exercise (AME; ref. 44). These ”post-RCP” scenarios were selected to extend the RCP/EMF-21 scenario space as much as possible. All scenarios, IAMs, and corresponding values for $[CO_2]^{2100}$ and RF_{NC}^{2100} are listed in Table S3.

21^{st} century emissions of the major anthropogenic greenhouse gases (CO_2, CH_4, N_2O, SF_6, and several halocarbons), aerosols and tropospheric ozone precursors (SO_2, CO, NO_x, and volatile organic compounds (VOC)) are specified in the scenarios, except for the AME scenarios which provide emissions only for CO_2, CH_4, and N_2O. In order to use the AME scenarios in our framework, we chose the most conservative approach by holding constant the aerosol emissions at the level of the year 2005 and neglecting the contribution from the missing minor greenhouse gases. Fossil-fuel (FF) CO_2 emissions are harmonized with the historical record[45] by cubic spline interpolation between the years 2010 and 2020. From this we calculate the radiative forcing from non-CO_2 greenhouse gases ($RF_{NC,GHG}$) and aerosols ($RF_{NC,aerosols}$) as described in refs. 17, 46. $RF_{NC} = RF_{NC,GHG} + RF_{NC,aerosols}$ is harmonized with the radiative forcing from historical emissions by the year 2005 as specified for the RCPs. CO_2 emissions are not included in the RF_{NC} calculation because they are used directly to force the interactive carbon cycle-climate model. For the concentration-driven simulations we obtain the CO_2 concentration pathway by diagnosing $[CO_2]$ in Bern3D-LPJ simulations with the standard parameter values and specified CO_2 emissions. Following the approach of ref. 47 for RCP4.5 and RCP6.0, we extend the scenarios from 2100 to 2300 by stabilizing $[CO_2]$ and RF_{NC} by the year 2150. We note that this approach might be somewhat too pessimistic for low emission scenarios. The resulting forcing time series are shown in Fig. S4 together with the corresponding FF-CO_2 emissions for the standard model parameter settings.

In addition to $[CO_2]$ (or FF-CO_2 for the emission-driven simulations) and RF_{NC}, the Bern3D-LPJ model is forced with CMIP5 (ref. 48) recommended data sets of anthropogenic land-use changes[49], volcanic aerosols[50], solar irradiance[51,52], and orbital configuration[13]. After 2005, no volcanic forcing is applied, the orbital forcing remains constant, and the last solar cycle is repeated. After 2100, the land-use area is assumed to remain constant. This experimental setup is very similar to that of refs. 1, 2. Since land-use maps are only available for the four

RCP scenarios, the other 51 scenarios assume 21st century land-use changes according to the RCP8.5 scenario.

We have examined the sensitivity of the results to the choice of the land-use maps with simulations where the land-use maps from all four RCPs are applied to each EMF-21 scenario. These simulations are carried out with a model setup where the parameters are set to the median of the posterior parameter distributions. This model configuration reproduces the median of the ensemble reasonably well (black crosses in Fig. S19). We find that prescribing the land-use map from RCP2.6 instead of RCP8.5 has a negligible effect on the diagnosed FF-CO_2 emissions (-1 to -3 GtC; Fig. S19a) and ΔSAT (-0.01 to 0.02 °C; Fig. S19b). Effects are larger when prescribing the land-use maps from RCP4.5 or RCP6.0. This is not surprising as in RCP8.5 and RCP2.6 the total global land-use area is increasing in a similar way similarly during the 21st century[40], leading to cumulative land-use change emissions of the same order of magnitude. In contrast, the total land-use area decreases in RCP4.5 and RCP6.0 and the cumulative land-use change emissions are hence lower. Our sensitivity runs show that the diagnosed FF-CO2 emissions are 50–60 GtC (RCP6.0 land-use) and 90–100 GtC (RCP4.5 land-use) higher than when prescribing RCP8.5 (or RCP2.6) land-use maps (Fig. S19a). That means that the allowable emissions shown e.g. in Fig. 4 of the paper would be somewhat higher (about 5–10% for the mid-range scenarios) when assuming that the land-area decreases in the 21st century as in the RCP4.5 and RCP6.0 scenarios. The effect on the global mean temperature change due to different land surface albedo is very small (0.04–0.06 °C for RCP6.0 and 0.07–0.09 °C for RCP4.5; Fig. S19b). The sea-level rise and ocean acidification targets are not affected by different land-use maps (or only indirectly via SAT). The cropland targets are neither affected because we only account for changes on present-day (2000 A.D) cropland areas.

Atmospheric CFC-11 (ref. 53) and ^{14}C (refs. 54–56) concentrations are specified for the historical period to simulate the air-sea gas transfer and ocean mixing of these tracers. Tracer distributions of CFC-11 and ^{14}C in the ocean are only needed to constrain the model ensemble and the specified atmospheric concentrations are independent from [CO_2], radiative forcing, or other model components.

Calculation of allowable emissions

To derive the Complementary Cumulative Distribution Function (CCDF) of allowable cumulative fossil-fuel emissions as shown in Figs. S14 to S18 we need to extend the simulation results from the limited set of scenarios to the whole scenario space spanned by these scenarios. We represent the scenario space as two-dimensional space with coordinates ($[CO_2]^{2100}$, RF_{NC}^{2100}). The model simulations provide results for the 55 corresponding points in that space. By using ordinary kriging[57] we interpolate all required variables of each ensemble member on a regular 200×200 grid inside the convex hull of these points. This is done for the 26 RCP and EMF-21 scenarios as well as for the extended set with all 55 scenarios.

In the next step, we search for the isolines in the interpolated fields that correspond to the defined limits for the selected target variables. If we consider multiple targets simultaneously, we accordingly search for the grid cells in the scenario space that define the boundary of the region where none of the targets is exceeded. We require that the target limit is never exceeded up to 2100 (or 2300) and therefore we analyze the maximum of the target variables for the time horizons 2005–2100 and 2005–2300, respectively. This is a stronger requirement than just demanding that the limit is not exceeded at the year 2100 or 2300. In many cases, however, the two options are equivalent because the target variables are strictly increasing with time. An exception is, for example, $A_{\Omega>3}$ in the RCP2.6 scenario, where the loss of surface waters with $\Omega_{\mathrm{arag}} > 3$ peaks before 2100 and decreases afterwards to values similar as today by 2300 (Fig. S1)

The grid cells of the interpolated cumulative FF-CO_2 emissions that correspond to the isoline for a specific target then define the allowable emissions for this target (c.f. isolines in Fig. 3). To capture the scenario uncertainty introduced by the range of RF_{NC}^{2100} for a given $[CO_2]^{2100}$ we determine the maximum ($E_{t,m}^{\mathrm{a,max}}$), minimum ($E_{t,m}^{\mathrm{a,min}}$), and average ($E_{t,m}^{\mathrm{a,ave}}$) allowable emissions along the isoline for each target t and ensemble member m.

No isoline can be found if all scenarios yield higher or lower values than the target limit. In that case, we cannot determine the allowable emissions, but it is clear that they must be lower than the emissions in the lowest scenario ($E_m^{\mathrm{s,min}}$) if all scenarios exceed the limit, or higher than the emissions of the highest scenario ($E_m^{\mathrm{s,max}}$) if no scenario exceeds the limit, respectively. We handle this problem by excluding an ensemble member from the CCDF outside of the range $E_m^{\mathrm{s,min}}$–$E_m^{\mathrm{s,max}}$ if the allowable emissions cannot be determined. Portions of CCDFs where more than 10% of the total model weight had to be excluded due to this reason are shown as symbols without uncertainty range in Fig. 4 and as dashed lines in Figs. S14 to S18, respectively. Generally, this indicates that the corresponding target is too low (or too high) to make a sound quantitative statement for the concerning range of emissions because this range lays outside of the range of scenarios considered here. The given emissions can therefore be interpreted as estimates for upper (lower) limits in those cases.

Finally, the CCDF for each target t is determined from the entire ensemble as

$$\mathrm{CCDF}_t^{\mathrm{max/min/ave}}(E) = \sum_m \theta(E_{t,m}^{\mathrm{a,max/min/ave}} - E)\hat{S}_m \quad (6)$$

$$\theta(x) = \begin{cases} 0 & \text{if } x < 0 \\ 1 & \text{if } x \geq 0, \end{cases} \quad (7)$$

where $\hat{S}_m = \frac{S_m}{\sum_m S_m}$ is the normalized score of the ensemble members that contribute to that portion of the CCDF as explained above. $\mathrm{CCDF}_t^{\mathrm{ave}}(E)$ is shown as lines in Fig. S14, $\mathrm{CCDF}_t^{\mathrm{min}}(E)$ and $\mathrm{CCDF}_t^{\mathrm{max}}(E)$ define the shaded areas. The results presented in Fig. 4 are obtained by evaluating $\mathrm{CCDF}_t^{\mathrm{ave}}(E)$, $\mathrm{CCDF}_t^{\mathrm{min}}(E)$ and $\mathrm{CCDF}_t^{\mathrm{max}}(E)$, at the 66% and 90% confidence levels, respectively.

Supplementary Tables S1 to S5

Table S1: **Sampled model parameters.**

Comp.	Parameter	Description	p_{std}	p_{min}	p_{max}	Prior[a]	p_{post} [5%,95%][b]	Refs.
LPJ	α_a	Photosynthesis scaling parameter (leaf to canopy)	0.5	0.3	0.7	$N(p_{std}, \sigma)$	0.49 [0.34,0.67]	28, 58
	α_{C_3}	Intrinsic quantum efficiency of CO_2 uptake (C_3 plants)	0.08	0.02	0.125	$N(p_{std}, \sigma)$	0.07 [0.04,0.10]	20, 28, 59
	$\theta^\star = 1 - \theta$	Co-limitation shape parameter (light vs. Rubisco act.)	0.3	0.004	0.8	$L(p_{std}, 0.54, 0)$	0.31 [0.13,0.78]	28, 60, 61
	g_m	Max. canopy conductance [c]	3.26	2.5	18.5	$L(p_{std}, 1.05, 1.5)$	2.89 [1.78,8.00]	28, 62
	$\tau_{sapwood}$	Sapwood to heartwood turnover (yr)	20	5	100	$L(p_{std}, 0.76, 0)$	19.9 [5.5,71.1]	28, 63
	$mort_{max}$	Asymptotic maximum mortality rate (yr^{-1})	0.01	0.005	0.1	$L(p_{std}, 1.19, 0)$	0.02 [0.01,0.06]	28
	$resp_{Q_{10},eq}$	Temp. sensitivity of respiration and soil decomp[d]	2.4	1.3	3.3	$N(p_{std}, \sigma)$	2.27 [1.48,3.04]	29, 64
	$k_{soil,scale}$	Scaling factor for SOM decomp. rates at 10 °C	1.0	0.5	2.0	$L(p_{std}, 0.41, 0.2)$	1.06 [0.62,1.86]	65
	f_{soil}	Fraction of decomp. litter entering soil pools (%)	40	20	60	$N(p_{std}, \sigma)$	38.3 [14.2,66.0]	28, 66
	f_{slow}	Fraction of soil-bound litter entering slow soil pool (%)	1.5	1.0	15	$L(p_{std}, 1.05, 0)$	1.18 [0.22,5.92]	28, 67
	$C_{peat,scale}$	Initial soil carbon in NH peatlands (GtC)	420	190	650	$N(p_{std}, \sigma)$	458 [234,653]	68
EBM	CS	Nominal[e] equilibrium climate sensitivity (°C)	3	1	10	$L(p_{std}, 0.58, 0)$	2.2 [1.0,5.1]	69, 70
	$diff_{zonal}$	Zonal atmospheric eddy-diffusivity (10^6 m^2 s^{-1})	1.0	0.1	10	$L(p_{std}, 1.06, 0)$	0.9 [0.2,6.2]	11
	$diff_{merid,scale}$	Scaling factor for meridional atm. eddy-diffusivity	1.0	0.5	2.0	$L(p_{std}, 0.34, 0)$	1.0 [0.6,1.7]	11
OCN	$diff_{dia}$	Ocean diapycnal diffusivity (10^{-5} m^2 s^{-1})	1.0	0.2	20	$L(p_{std}, 1.35, 0)$	2.18 [0.21,12.8]	70, 71
	$diff_{iso}$	Ocean isopycnal diffusivity (m^2 s^{-1})	1,000	300	9,000	$L(p_{std}, 1.01, 0)$	1,380 [294,7,668]	71, 72
	$k_{gas,scale}$	Scaling factor for standard OCMIP gas transfer velocity	0.81	0.65	0.97	$N(p_{std}, \sigma)$	0.82 [0.67,0.95]	31
FOR	$RF_{GHG,scale}$	Scaling factor for total RF from well mixed GHG	1.0	0.92	1.12	$L(p_{std}, 0.17, 0.7)$	0.99 [0.93,1.09]	32
	$RF_{aerosol,scale}$	Scaling factor for total aerosol RF	1.0	0.5	2.0	$L(p_{std}, 0.35, 0)$	1.09 [0.66,1.76]	32

[a]The prior normal, $N(p_{std}, \sigma)$, and log-normal, $L(p_{std}, s, l)$ distributions are selected such that the median matches the standard model parameter value (p_{std}) and the standard-deviation $\sigma = \frac{p_{max} - p_{min}}{4}$ (see text and Fig. S2).

[b]Posterior median and [5%,95%]-percentiles of the parameter PDF from the constrained ensemble.

[c]Empirical parameter for the atmospheric water demand function.

[d]Arrhenius-type dependence that corresponds to the given Q_{10} value for moderate temperatures.

[e]The equilibrium climate sensitivity is not an explicit model parameter in Bern3D. Instead, a feedback parameter is adjusted to match the given CS value approximately (see text).

doi:10.1038/nature12269

Table S2: **Observation-based data sets used to constrain the model ensemble.** See also Fig. S3.

Group	Subgroup	Variable	Time/region	References
Land	Fluxes	Seasonal CO_2 (GLOBALVIEW-CO_2)	Average seasonal cycle at nine sites.	73
		fAPAR[a] (SeaWiFS)	Seasonal climatology (2-D field)	74
		NPP (EMDI class A)	Estimates from about ~80 sites worldwide.	75
		NPP (FLUXNET)	Estimates from about ~140 sites worldwide.	76
	Soil C	Low/mid-latitude soil carbon content	2-D field south of 50°N	77
		High latitude soil carbon content	2-D field North America, north of 50°N	68, 78
		Global soil carbon content	Global inventory 1,950±550 GtC (1σ)	79
	Veg. C	Vegetation carbon	Estimates from ~140 sites worldwide.	76
		Vegetation carbon	Estimates from ~140 sites worldwide.	80
		Global vegetation carbon	Global inventory 550±200 GtC (1σ, preind.)	81
Ocean	WOA[b]	Temperature (T)	Surface (2-D) and 3-D climatological fields	82
		Salinity (S)	Surface (2-D) and 3-D climatological fields	83
		Phosphate (PO_4)	Surface (2-D) and 3-D climatological fields	84
	GLODAP[c]	Alkalinity (Alk)	Surface (2-D) and 3-D fields (1995)	85
		CFC-11	Surface (2-D) and 3-D fields (1995)	85
		Dissolved inorganic carbon (DIC)	Surface (2-D) and 3-D fields (preindustrial)	85
		^{14}C	Surface (2-D) and 3-D fields (preindustrial)	85
CO_2	Atm. record	[CO_2] from ice-core analysis	Time series 1850-1958	86
		Direct [CO_2] measurements	Time series 1959-2010	87, 88
	Uptake rates	Net ocean carbon uptake rates	Global mean 1959-2006, 1990-1990, and 2000-2006	89
		Net land carbon uptake rates	Global mean 1959-2006, 1990-1990, and 2000-2006	89
Heat	SAT anomaly	Northern hemisphere SAT (HadCRUT3)	Annual mean time series 1850-2010	90
		Southern hemisphere SAT (HadCRUT3)	Annual mean time series 1850-2010	90
	Ocean heat	Ocean heat content anomaly	Global mean time series 1955-2011 (0-700 m)	91
		Ocean heat content anomaly	Global mean time series 1993-2008 (0-700 m)	92
		Ocean heat uptake	Global mean 2005-2010	93

[a]Fraction of absorbed photosynthetically active radiation.

[b]World Ocean Atlas 2009, http://www.nodc.noaa.gov/OC5/WOA09/pr_woa09.html

[c]Global Ocean Data Analysis Project, http://cdiac.ornl.gov/oceans/glodap/

doi:10.1038/nature12269

Table S3: **Emission scenarios from the EMF-21[41], RCP[39], IIASA GGI[43], and AME[44] integrated assessment modeling projects used to generate the forcing time series for the scenario simulations (Fig. S4)**. The mitigation scenarios are based on radiative forcing targets (OS = overshoot is allowed, NTE = not-to-exceed), [CO_2] stabilization targets, or a global carbon price, rising at 5% per year. Corresponding SRES-storylines are given in brackets where applicable. The GGI and AME scenarios used in this study were selected from larger set of 20 and 64 scenarios, respectively. The AME scenarios provide emissions only for the three major greenhouse gases CO_2, CH_4, and N_2O and are therefore characterized by a low RF_{NC} in this study (see text).

No	Project	Model	Scenario	$[CO_2]^{2100}$	RF_{NC}^{2100}	
				(ppm)	Total (W/m^2)	Aerosol (W/m^2)
1	EMF-21	AIM	4.5 W/m^2 (B2)	632	0.74	-0.70
2			Reference (B2)	790	1.78	-0.77
3		EPPA	4.5 W/m^2	671	1.13	-0.81
4			Reference	1,030	2.82	-1.19
5		IMAGE	2.6 W/m^2 (B2)	439	0.77	-0.12
6			2.9 W/m^2 (B2)	485	0.76	-0.11
7			3.7 W/m^2 (B2)	530	1.00	-0.10
8			4.5 W/m^2 (B2)	642	0.98	-0.21
9			5.3 W/m^2 (B2)	714	0.88	-0.43
10			Reference (B2)	853	1.18	-0.70
11		IPAC	4.5 W/m^2 (B2)	644	1.54	-0.35
12			Reference (B2)	852	1.96	-0.55
13		MESSAGE	3.2 W/m^2 (B2)	503	1.43	-0.27
14			4.5 W/m^2 (A2)	621	1.65	-0.42
15			4.6 W/m^2 (B2)	645	1.63	-0.30
16			Reference (A2)	1,114	3.34	-0.71
17			Reference (B2)	795	2.36	-0.43
18		MiniCAM	3.5 W/m^2 (B2)	484	0.65	-0.30
19			4.0 W/m^2 (B2)	541	0.70	-0.29
20			4.5 W/m^2 (alt,B2)	604	0.77	-0.27
21			4.5 W/m^2 (emf,B2)	616	0.75	-0.28
22			Reference (B2)	860	1.29	-0.38
23	RCP	IMAGE	RCP2.6	459	0.85	-0.14
24		MiniCAM	RCP4.5	575	0.97	-0.28
25		AIM	RCP6	763	1.15	-0.23
26		MESSAGE	RCP8.5	1,119	2.25	-0.30

Continued on next page

Table S3 – *Continued from previous page*

No	Project	Model	Scenario	$[CO_2]^{2100}$ (ppm)	RF_{NC}^{2100} Total (W/m^2)	RF_{NC}^{2100} Aerosols (W/m^2)
27	GGI	MESSAGE	450ppm (A2r)	445	1.35	-0.33
28			450ppm (B2)	479	1.40	-0.26
29			590ppm (A2r)	565	1.52	-0.44
30			820ppm (A2r)	736	1.77	-0.46
31			1090ppm (A2r)	965	1.87	-0.69
32			Reference (B1)	698	2.00	-0.14
33	AME	AIM-CGE	CO_2 price \$10 (5% p.a.)	578	0.32	-1.17
34			Reference	1,088	0.47	-1.17
35		EPPA	CO_2 price \$10 (5% p.a.)	711	0.32	-1.17
36			CO_2 price \$30 (5% p.a.)	584	0.03	-1.17
37		GCAM	CO_2 price \$30 (5% p.a.)	439	0.19	-1.17
38			CO_2 price \$50 (5% p.a.)	394	0.18	-1.17
39		GRAPE	CO_2 price \$50 (5% p.a.)	506	0.63	-1.17
40			Reference	831	0.82	-1.17
41		GTEM	CO_2 price \$10 (5% p.a.)	657	0.13	-1.17
42			CO_2 price \$50 (5% p.a.)	475	-0.12	-1.17
43			Reference	1,151	0.91	-1.17
44		IMAGE	3.7 W/m^2 NTE	551	-0.06	-1.17
45			Reference	862	-0.11	-1.17
46		MERGE	CO_2 price \$10 (5% p.a.)	627	0.31	-1.17
47		MESSAGE	2.6 W/m^2 OS	468	0.26	-1.17
48		ReMIND	2.6 W/m^2 OS	443	-0.19	-1.17
49			CO_2 price \$50 (5% p.a.)	422	-0.10	-1.17
50			Reference	976	0.93	-1.17
51		TIAM-WORLD	CO_2 price \$30 (5% p.a.)	516	-0.10	-1.17
52			Reference	892	0.63	-1.17
53		TIMES-VTT	2.6 W/m^2 OS	482	-0.28	-1.17
54		WITCH	CO_2 price \$10 (5% p.a.)	672	0.18	-1.17
55			CO_2 price \$50 (5% p.a.)	510	0.16	-1.17

Table S4: **Comparison of allowable cumulative CO_2 emissions (66% probability) with previous studies.** Please note that the cumulative emissions are given for different time periods and that the targets are evaluated for different time horizons. Further, the previous studies also include CO_2 emissions from land-use change, which is excluded in the present study on purpose. Land-use related emissions in the 21st century are estimated on the order of ± 70 GtC for RCP2.6 and RCP4.5 (refs. 27, 49).

Target	Allowable cum. CO_2 emissions (GtC)	Time range	Reference
ΔSAT $< 2\,°$C	410 [370 – 440] (FF-CO_2 only)	2000–2100	This study (RCP, EMF-21, GGI)
	570 [360 – 750] (FF-CO_2 only)	2000–2100	This study (all scenarios)
	550 [300 – 770]	2000–2500	Zickfeld et al. (2009)[94]
	315 [220 – 410]	2000–2050[1]	Meinshausen et al. (2009)[70]
Multi-Target 2	320 [290 – 350] (FF-CO_2 only)	2000–2100	This study (all scenarios)
ΔSAT $< 3\,°$C	890 [690 – 1,060] (FF-CO_2 only)	2000–2100	This study (RCP, EMF-21, GGI)
	1,120 [690 – 1,540] (FF-CO_2 only)	2000–2100	This study (all scenarios)
	1,020 [700 – 1,300]	2000–2500	Zickfeld et al. (2009)[94]
Multi-Target 3	550 [460 – 600] (FF-CO_2 only)	2000–2100	This study (all scenarios)
ΔSAT $< 4\,°$C	1,380 [1,160 – 1,580] (FF-CO_2 only)	2000–2100	This study (RCP, EMF-21, GGI)
	1,610 [1,160 – 2,040] (FF-CO_2 only)	2000–2100	This study (all scenarios)
	1,450 [1,000 – 1,900]	2000–2500	Zickfeld et al. (2009)[94]
Multi-Target 4	1,060 [940 – 1,200] (FF-CO_2 only)	2000–2100	This study (all scenarios)

[1]Emissions are given for 2000–2050, but the temperature target is evaluated up to 2100.

doi:10.1038/nature12269

Table S5: **Implied limits on the additional target variables given by the temperature targets alone.** The implied limit for a target is the maximum in the subset of the scenario space that is compatible with a given temperature target. Results are given for the time horizons up to years 2100 and 2300, and when including/excluding the AME scenarios, respectively. The limits defined in multi-target sets 1 to 4 (Table 1) are given in the grey bars. If, e.g., the temperature target 3 °C alone is chosen, SSLR is projected to be within the range 14–36 cm up to year 2100 (AME scenarios excluded) and within 24–66 cm up to year 2300. For 2300, the median SSLR exceeds the SSLR limit of set 2, and the upper end of the range exceeds the SSLR limit of set 3. Like for allowable emissions, only an upper-limit estimate can be given in some cases (indicated with the '<' symbol).

		Implied limits given by the temperature target (median and 5–95% range)									
Time horizon	AME	SSLR (cm)		A_{SO} (%)		$A_{\Omega>3}$ (%)		$C_{\mathrm{NPP}>10\%}$ (%)		$C_{\mathrm{carbon\ loss}}$ (%)	
		1.5 °C temperature target									
2000–2100	excl.	< 15	[8–24]	< 6	[0–63]	< 91	[48–100]	< 4	[1–10]	< 7	[2–12]
	incl.	12	[0–22]	1	[0–66]	80	[0–100]	5	[0–12]	6	[0–12]
2000–2300	excl.	< 23	[13–38]	< 5	[0–58]	< 83	[42–100]	< 7	[1–14]	< 13	[5–19]
	incl.	< 22	[11–35]	< 6	[0–62]	< 90	[44–100]	< 14	[7–21]	< 14	[5–21]
Limits of target set 1:		20		5		60		5		5	
		2 °C temperature target									
2000–2100	excl.	< 18	[10–28]	< 8	[0–84]	< 96	[55–100]	< 5	[1–12]	< 8	[3–14]
	incl.	7	[6–27]	14	[0–97]	99	[29–100]	6	[1–13]	8	[0–15]
2000–2300	excl.	< 29	[17–46]	< 6	[0–82]	< 88	[47–100]	< 8	[2–15]	< 15	[5–23]
	incl.	28	[15–46]	13	[0–91]	97	[57–100]	14	[7–21]	15	[5–24]
Limits of target set 2:		40		10		75		10		10	
		3 °C temperature target									
2000–2100	excl.	23	[14–36]	37	[0–100]	100	[68–100]	5	[1–13]	10	[3–18]
	incl.	23	[13–36]	81	[9–100]	100	[87–100]	7	[2–14]	10	[3–18]
2000–2300	excl.	40	[24–66]	16	[0–100]	99	[55–100]	9	[2–17]	18	[5–29]
	incl.	40	[24–66]	53	[3–100]	100	[77–100]	14	[7–21]	18	[6–29]
Limits of target set 3:		60		25		90		20		20	
		4 °C temperature target									
2000–2100	excl.	28	[17–44]	88	[11–100]	100	[94–100]	6	[1–14]	11	[3–20]
	incl.	28	[17–43]	99	[44–100]	100	[100–100]	7	[2–14]	11	[3–20]
2000–2300	excl.	51	[33–85]	67	[1–100]	100	[65–100]	9	[2–19]	21	[7–34]
	incl.	51	[33–85]	95	[17–100]	100	[93–100]	14	[7–21]	22	[7–34]
Limits of target set 4:		80		50		100		30		30	

Supplementary Figures S1 to S19

doi:10.1038/nature12269

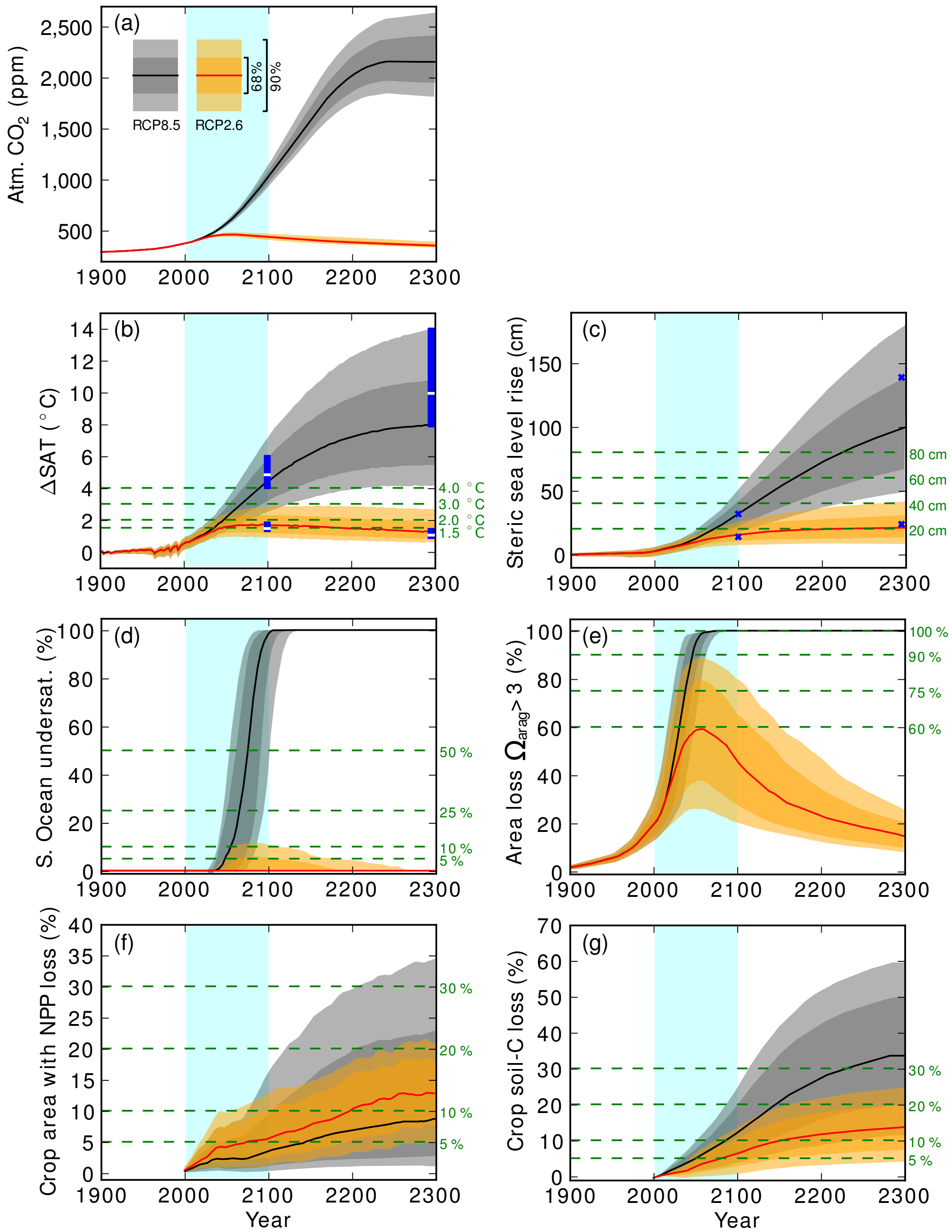

Figure S1: **Historical simulations and future projections to illustrate the response of the selected target variables.** Time series of $[CO_2]$ **(a)** and the six selected target variables **(b-g)** are shown for the high RCP8.5 (black) and the low RCP2.6 (red) emission scenario. The solid lines indicate the median of the constrained model ensemble and grey and yellow shadings represent the corresponding 68% (dark) and 90% (light) confidence intervals. The horizontal green lines indicate the four limits defined for each target variable and the blue shading indicates the main time horizon (2000–2100) investigated in this study. Recent estimates of ΔSAT [95] (blue bars; median and 66% range from probabilistic projection) and SSLR[96] (blue crosses; representative CMIP5 model) are shown for comparison. Cropland area with NPP loss are those areas where NPP decreases by more than 10% relative to 2005 A.D.

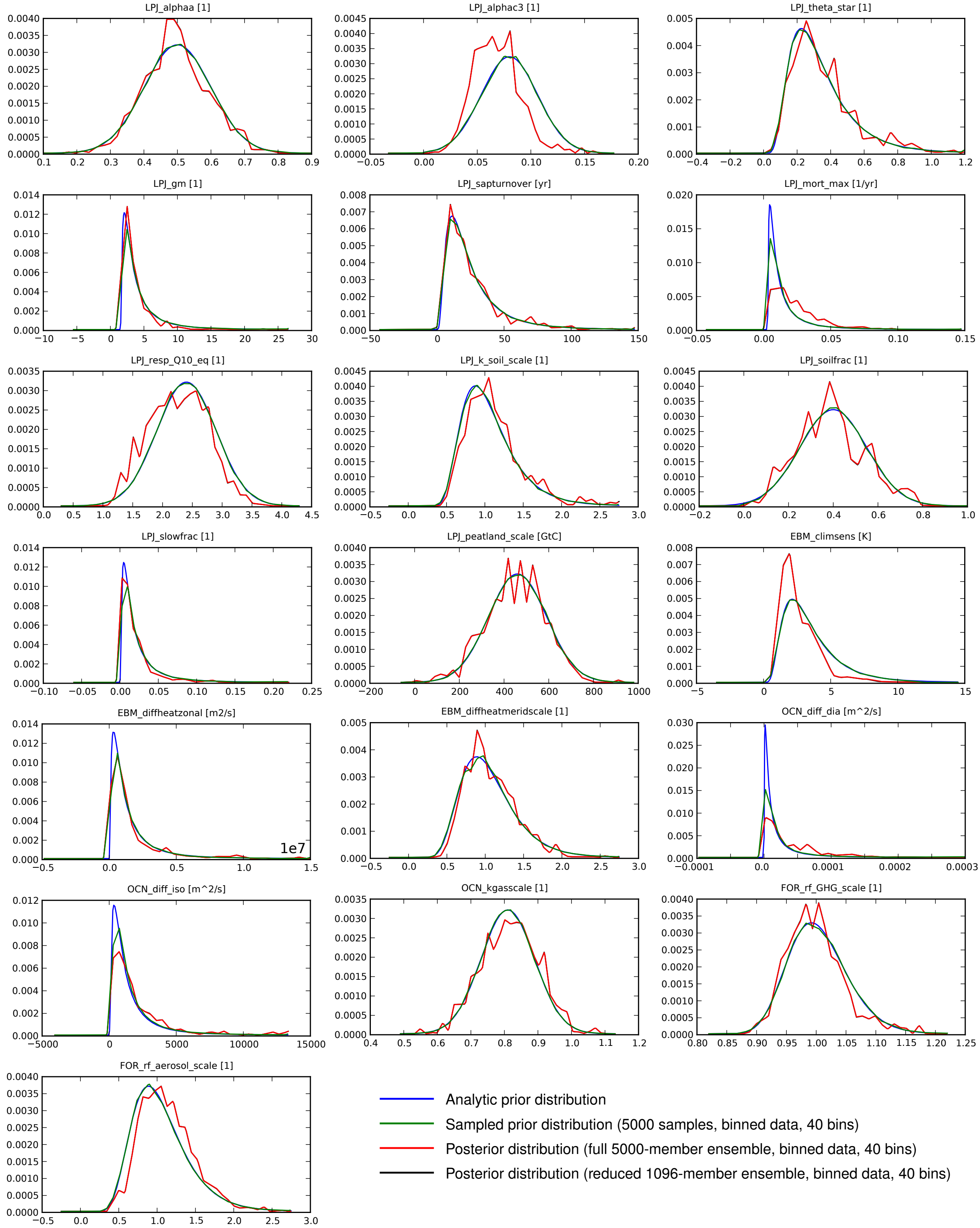

Figure S2: **Prior and posterior distributions of the 19 sampled model parameters (Table S1).** The specified analytic priors (Eq. 1-3) are shown in blue. The prior distributions derived from the actual samples (green) are binned (40 bins) in the same way as the posterior distributions (red) for comparison. The posterior distribution of the reduced 1,096-member ensemble (black) is virtually indistinguishable from the posterior of the full ensemble (red).

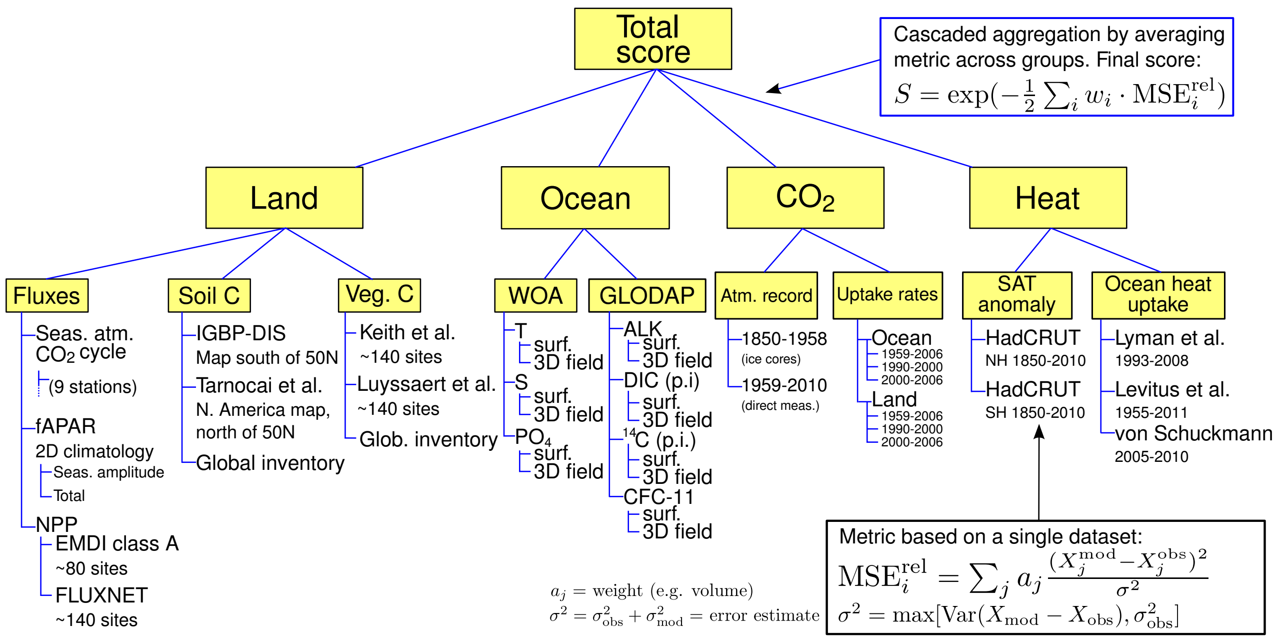

Figure S3: **Hierarchical structure of observation-based data (Table S2) used to constrain the model ensemble.**

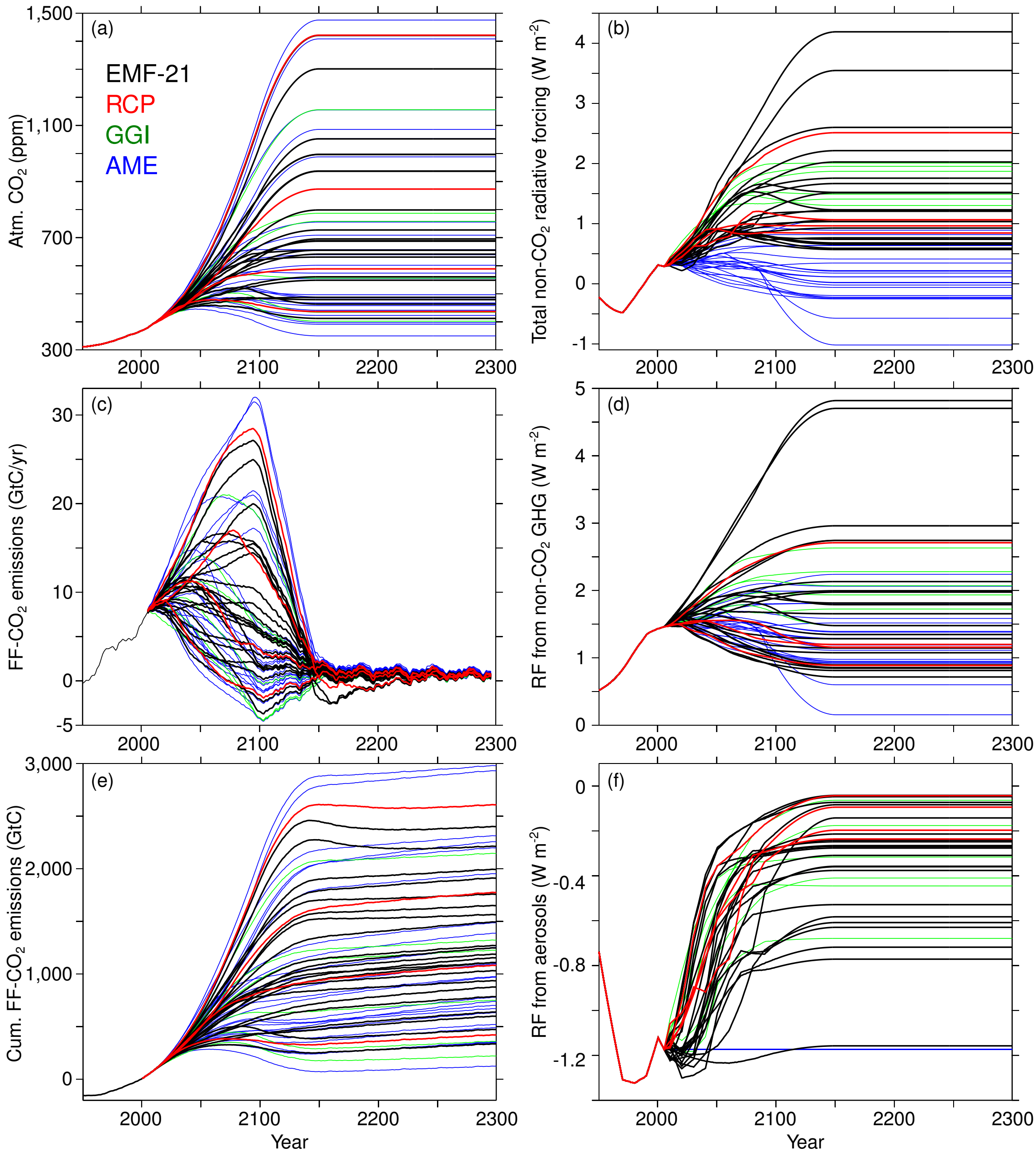

Figure S4: **Greenhouse gas scenarios.** **(a)** [CO_2] and **(b)** RF_{NC} are prescribed in the scenario simulations. The forcings are derived from 22 EMF-21 (black), 4 RCPs (red), 6 GGI (green), and 23 AME (blue) scenarios. After 2100 the scenarios are extended to 2300 by stabilizing [CO_2] and RF_{NC} by 2150. RF_{NC} is the sum of the forcing from **(d)** non-CO_2 greenhouse gases and **(f)** aerosols. Please note that for the AME scenarios the aerosol forcing is kept constant after 2005 because no aerosol emission paths are available for this scenarios. **(c)** Annual and **(e)** cumulative fossil-fuel CO_2 emissions diagnosed with the standard model parameter settings are shown for reference. The annual emissions are smoothed with a 10-year moving average filter. The cumulative emissions are given relative to the year 2000.

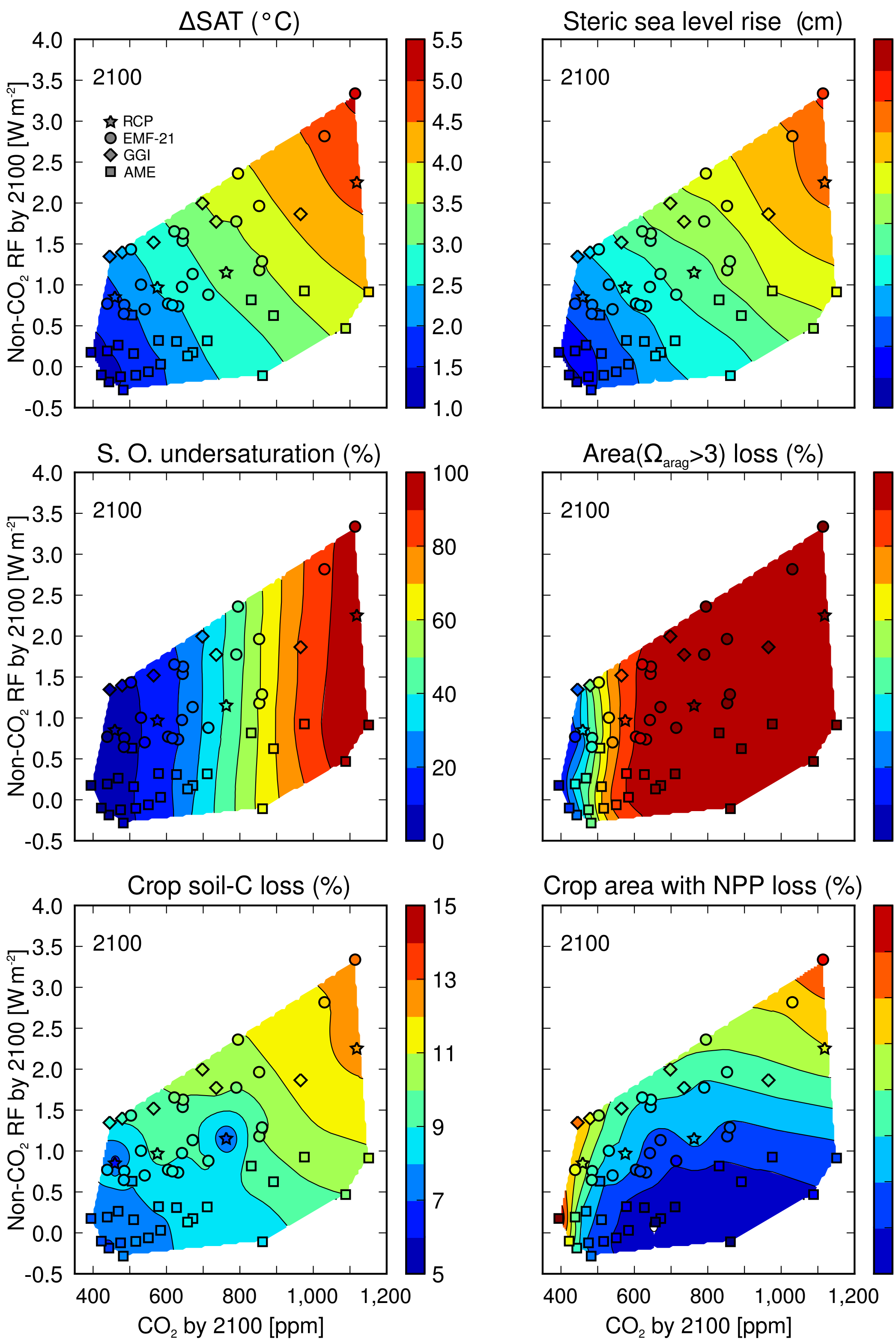

Figure S5: **Ensemble averages of the six target variables (maximum achieved in the 21st century), interpolated in the scenario space defined by $[CO_2]^{2100}$ and RF^{2100}_{NC}.** Symbols indicate the four RCPs (stars), 22 EMF-21 (circles), 6 GGI (diamonds), and 23 AME (squares) scenarios.

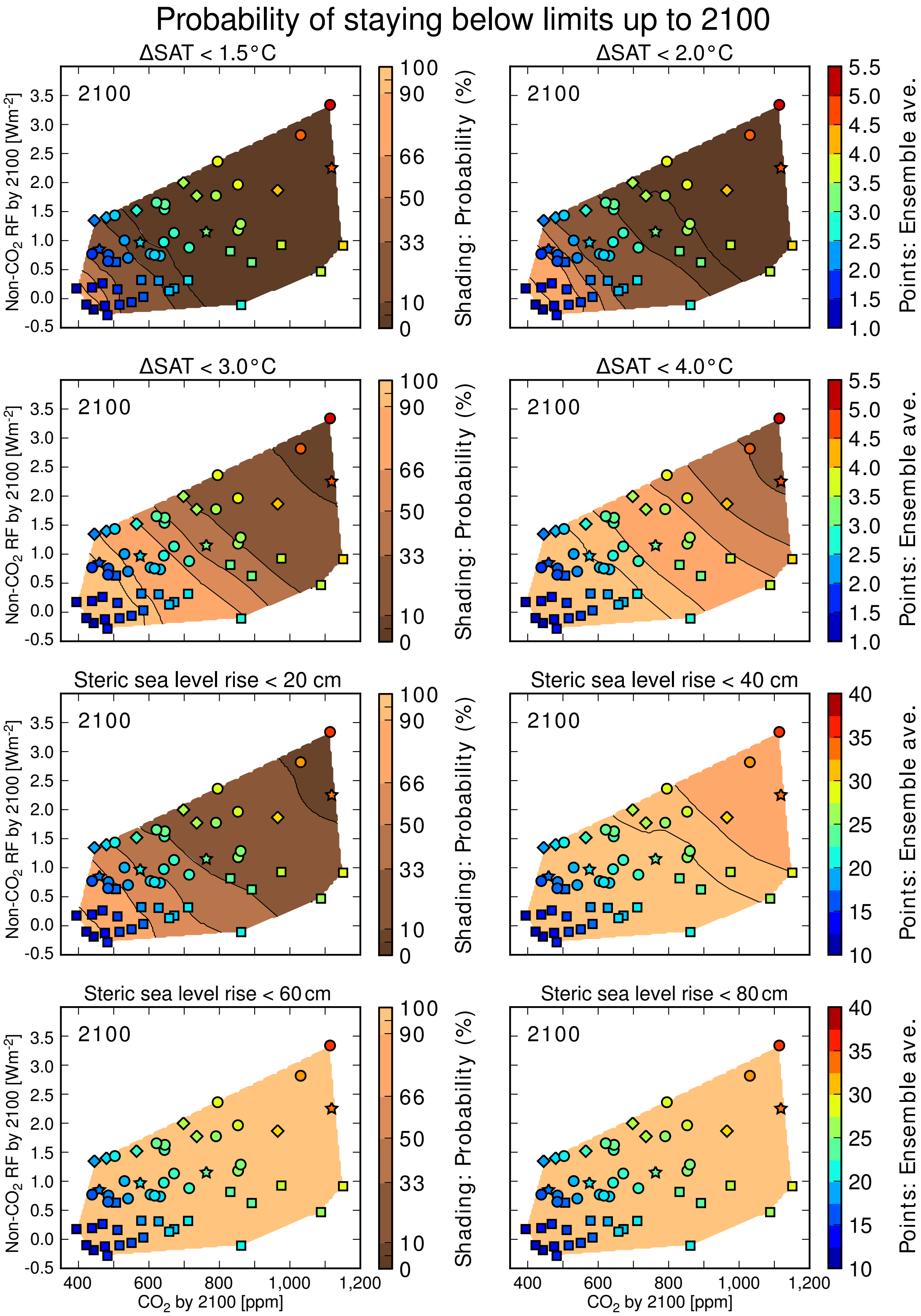

Figure S6: **As Fig. 2, but for all four limits of the two physical target variables.** The symbols indicate the ensemble average value of the corresponding target variable (max. 2000-2100) for the four RCPs (stars) and for each EMF-21 (circles), GGI (diamonds), and AME (squares) scenario.

doi:10.1038/nature12269

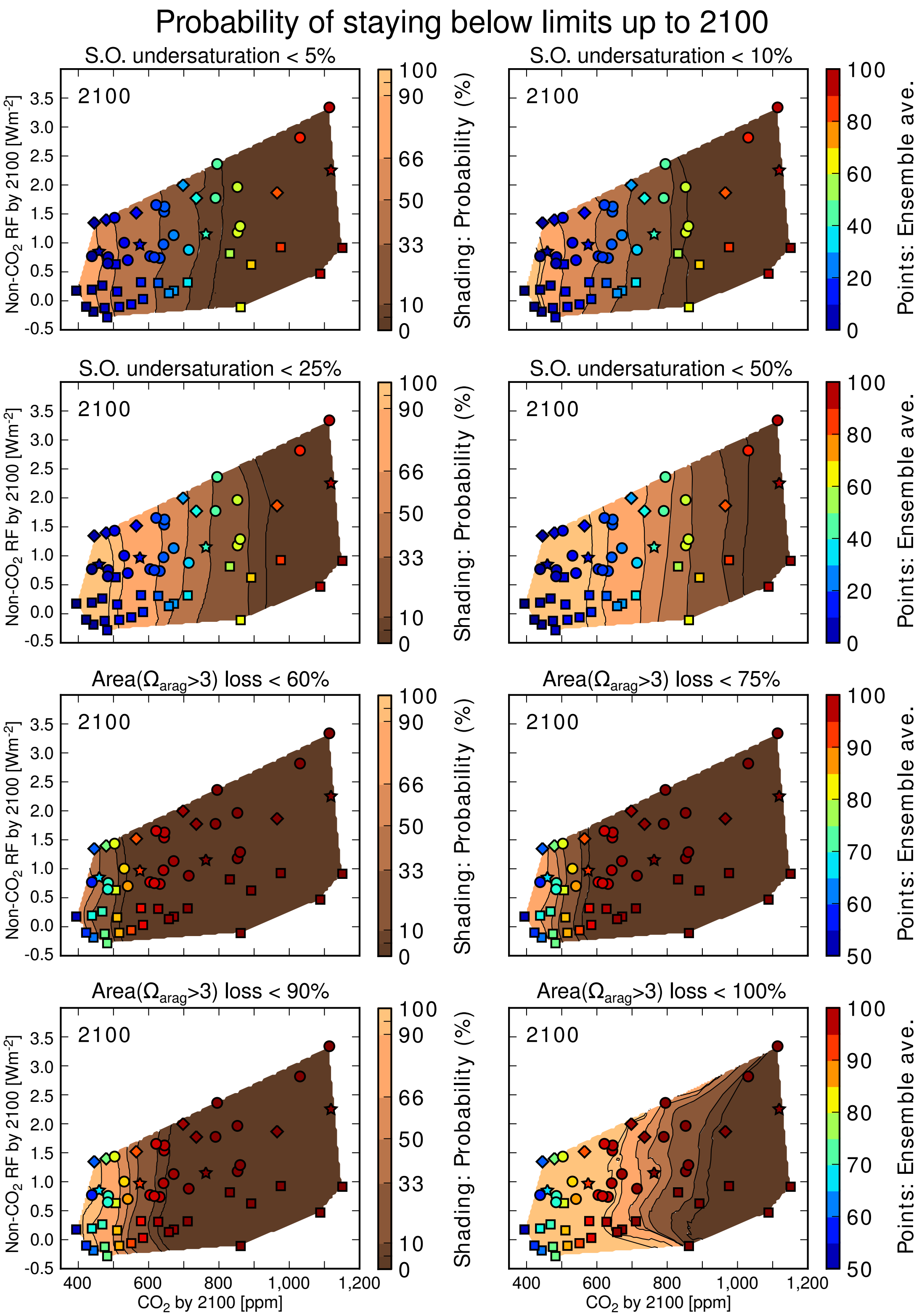

Figure S7: **As Fig. S6, but for the two OA target variables.**

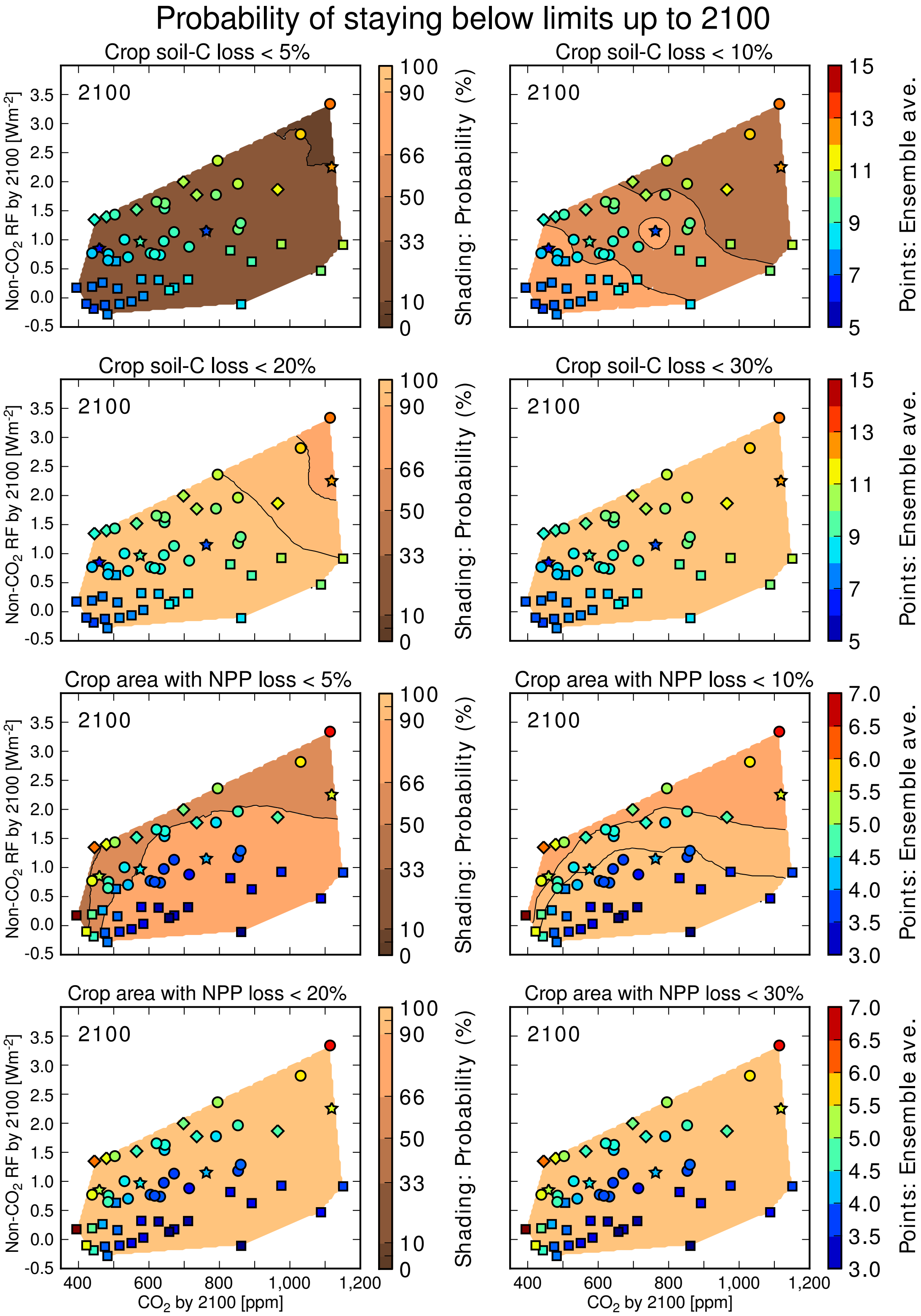

Figure S8: **As Fig. S6, but for the two cropland target variables.**

doi:10.1038/nature12269

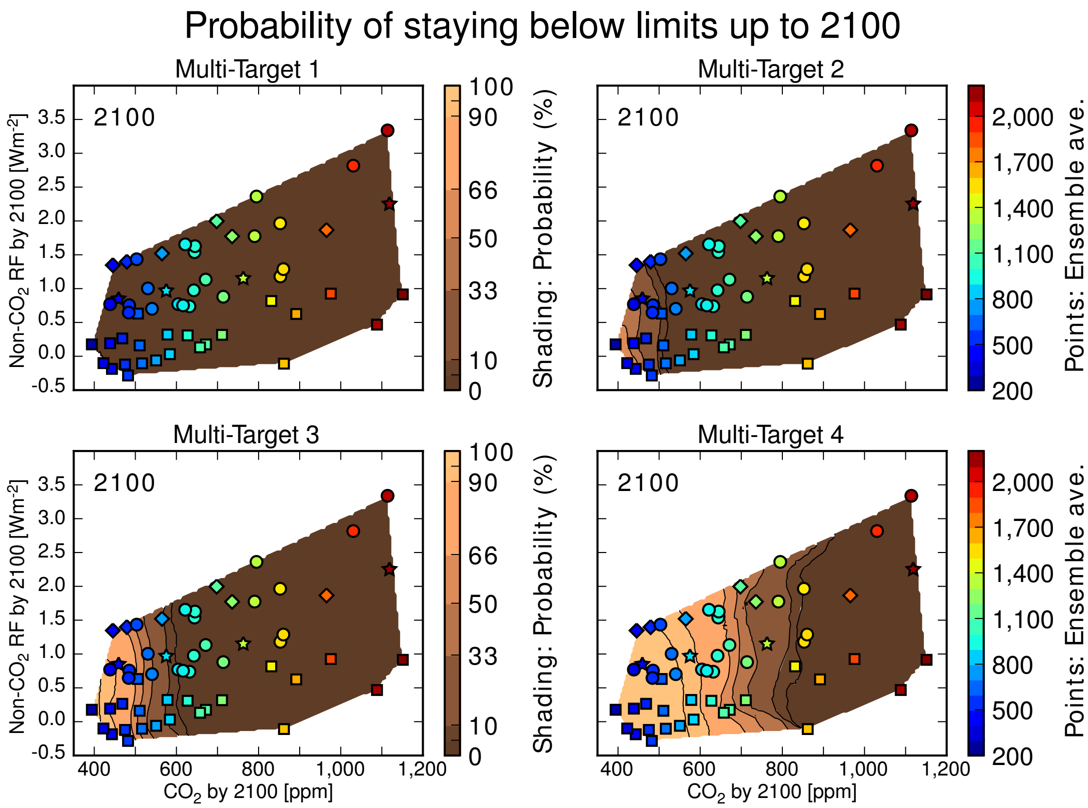

Figure S9: **As Fig. S6, but for the multi-targets.** The symbols show the ensemble mean cumulative fossil-fuel CO_2 emissions 2000-2100 (GtC).

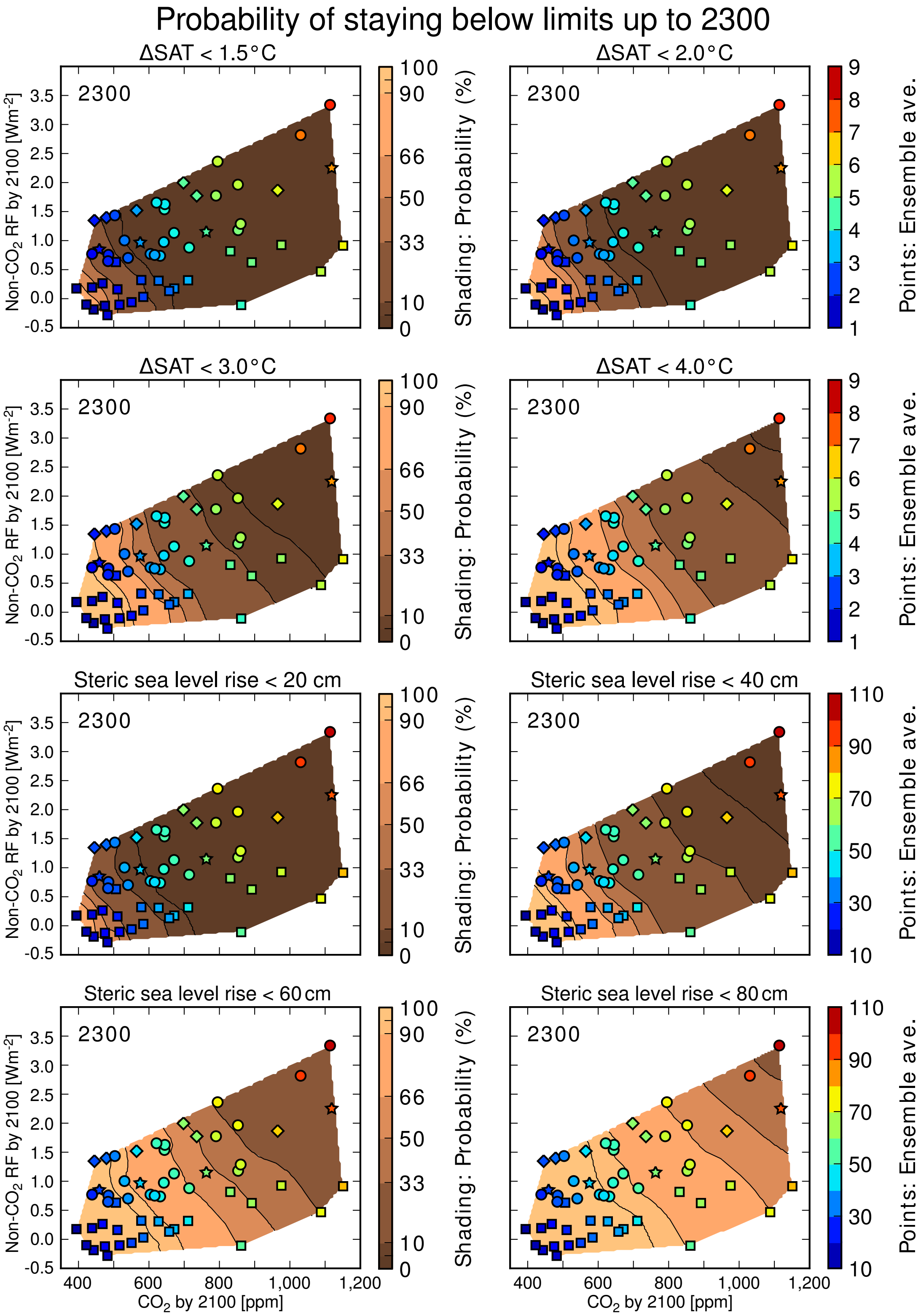

Figure S10: **As Fig. S6, but for the 2000-2300 time horizon.** The symbols indicate the ensemble average value of the corresponding target variable (max. 2000-2300) for the four RCPs (stars) and for each EMF-21 (circles), GGI (diamonds), and AME (squares) scenario.

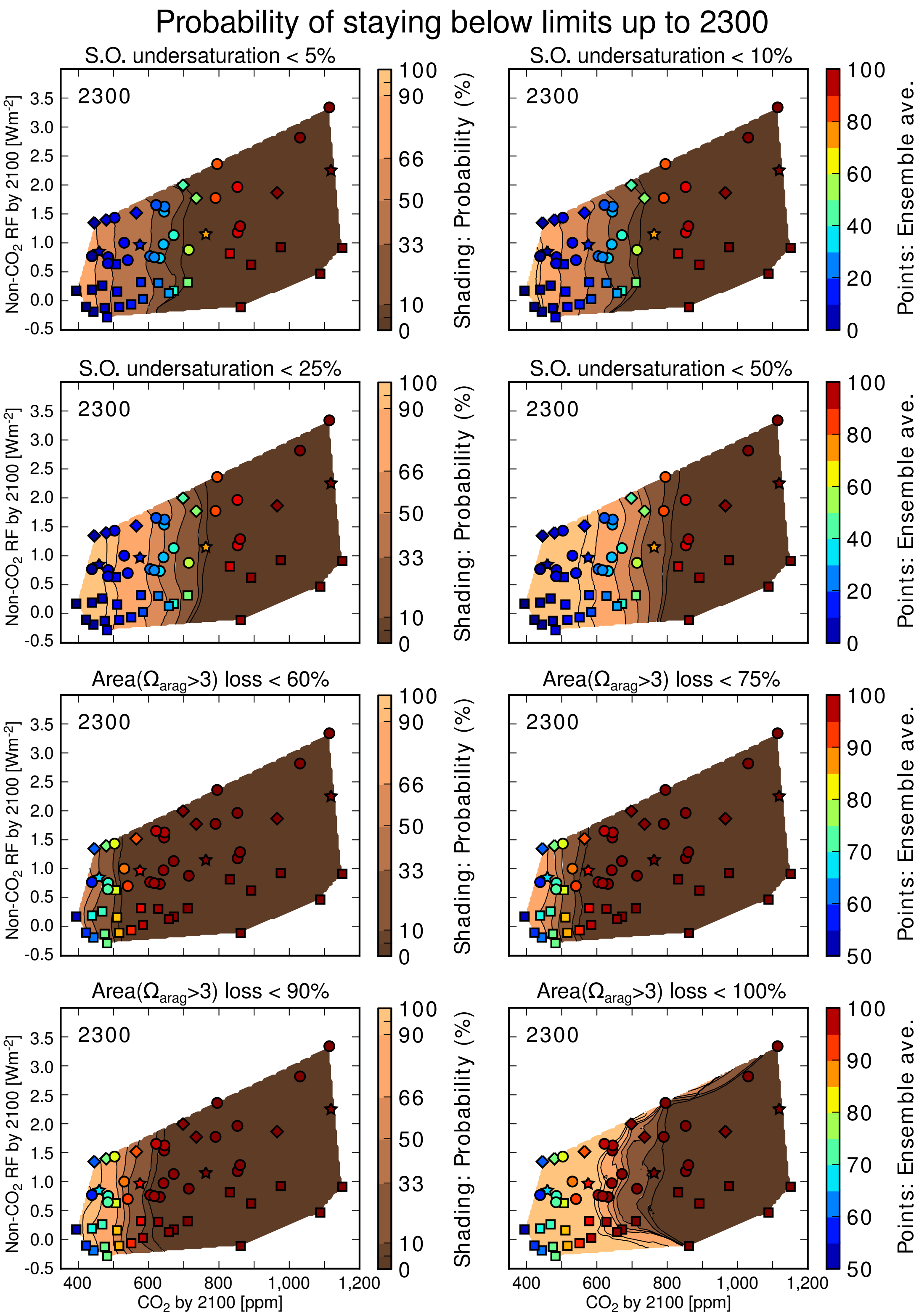

Figure S11: **As Fig. S10, but for the two OA target variables.**

doi:10.1038/nature12269

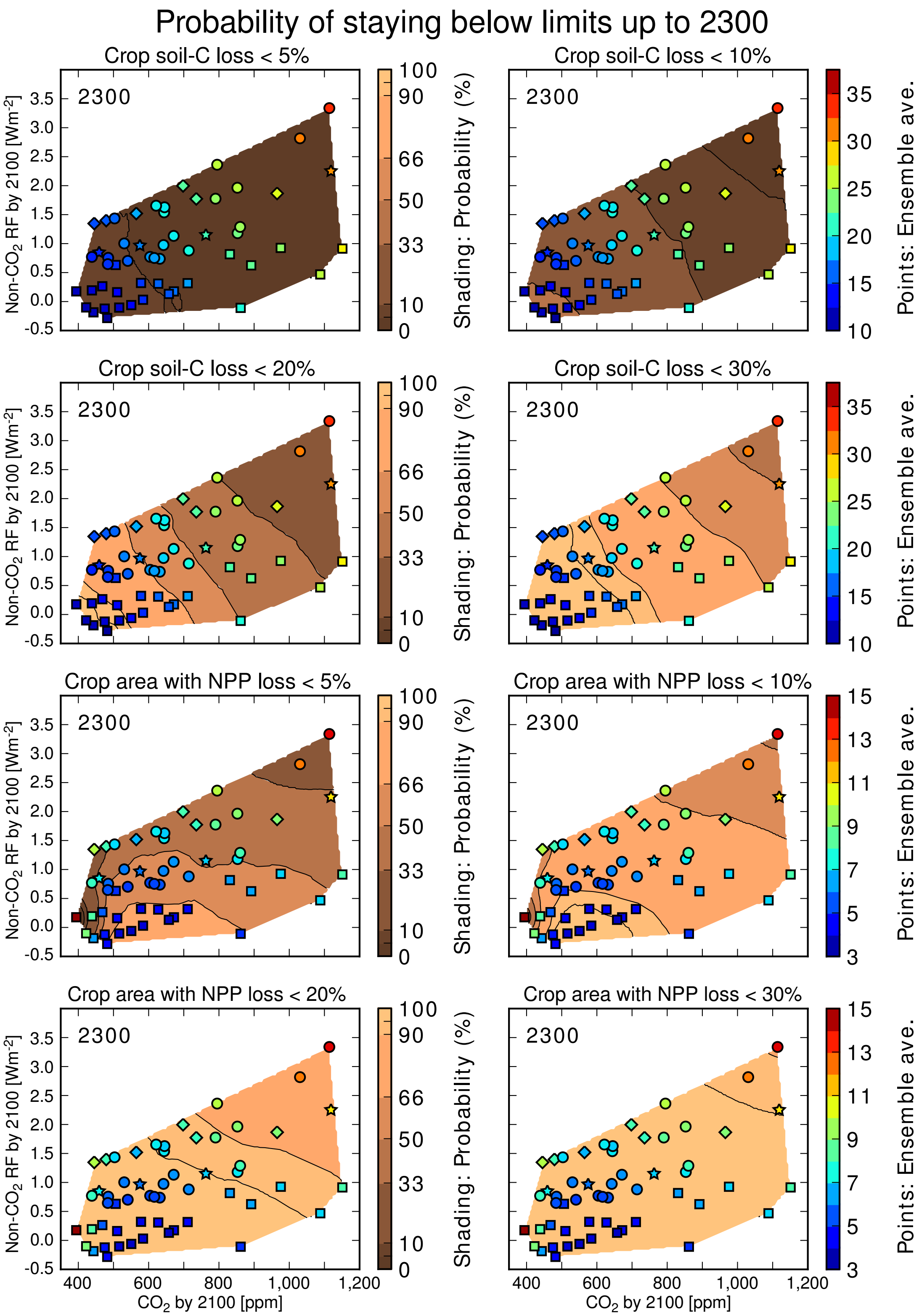

Figure S12: **As Fig. S10, but for the two cropland target variables.**

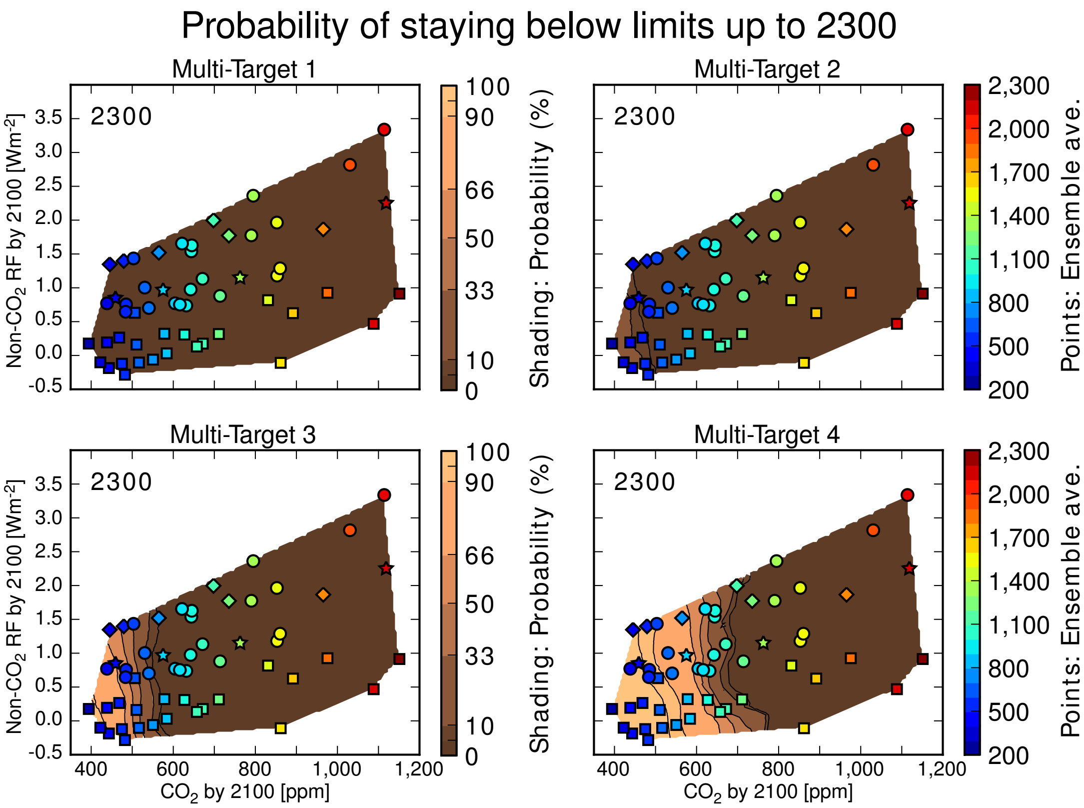

Figure S13: **As Fig. S10, but for the multi-targets.** The symbols show the ensemble mean cumulative fossil-fuel CO_2 emissions 2000-2100 (GtC).

doi:10.1038/nature12269

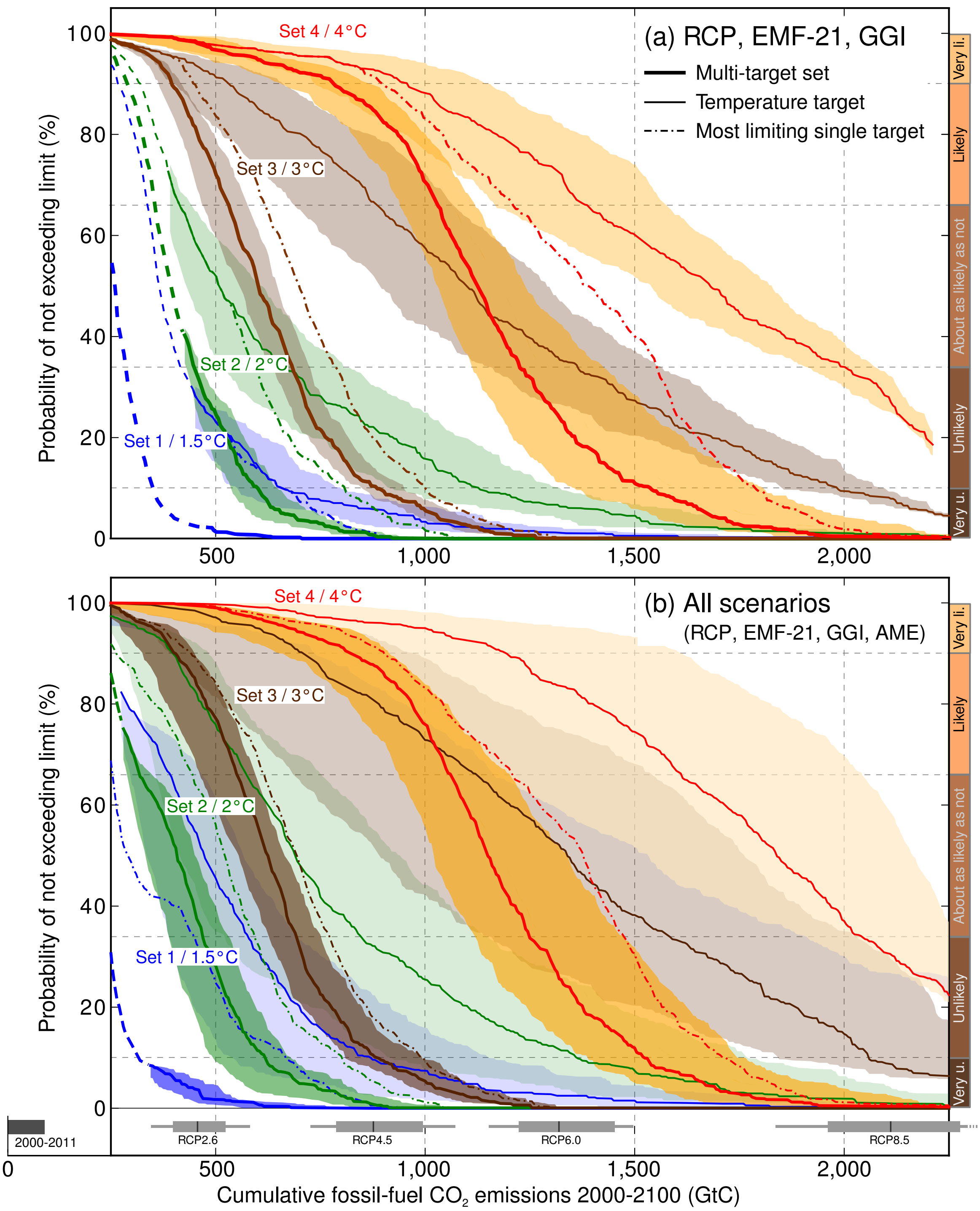

Figure S14: **Probability of staying below targets up to year 2100 as functions of cumulative fossil-fuel CO_2 emissions.** Results are given for the case when the AME scenarios with very low RF_{NC} are excluded **(a)** and also for the full scenario set **(b)**. Thin solid lines indicate the temperature targets and thick lines represent the corresponding multi-target sets. Shadings indicate the scenario uncertainty introduced by the range of RF_{NC} in the scenario space. Lines are dashed where the target limits lay outside of the examined scenario range in a significant number of model configurations (Methods). The dash-dotted lines show the results when considering the most limiting single target of a set. Historical emissions[97] and simulated emissions for the four RCP scenarios (median, 60% and 90% c.i.) are given above the x-axis.

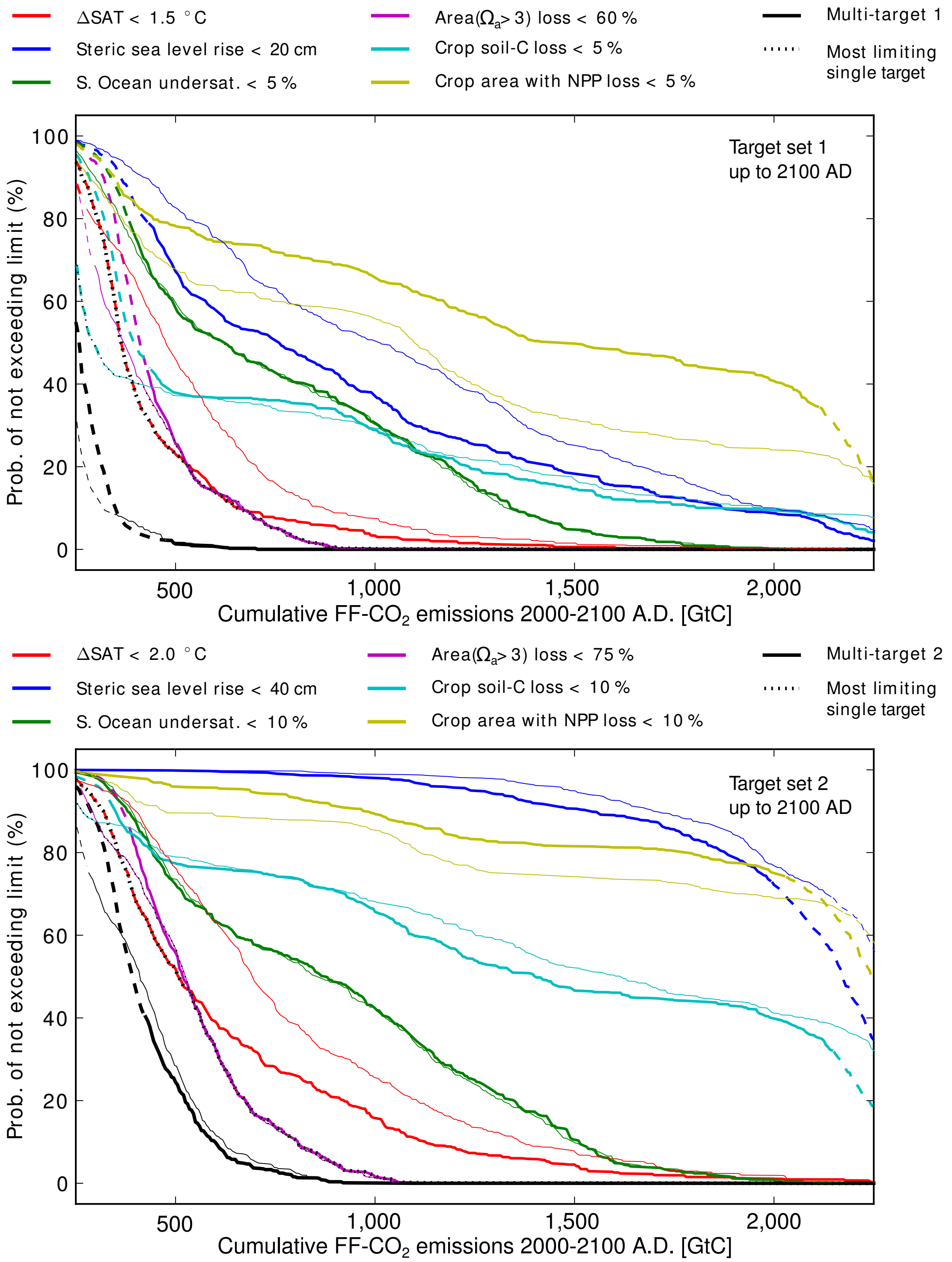

Figure S15: **As Fig. S14, but for all individual target variables.** The probability of not exceeding the defined limits in the 21st century is shown for the limits defined in set 1 (top) and set 2 (bottom). Results are given for the RCP, EMF-21, and GGI scenarios (thick lines) and also for all four scenario sets, including the AME scenarios with very low RF_{NC} (thin lines). The lines indicating the ΔSAT target (red), the multi-target (black), and the most limiting single target (black dotted line) are as shown combined for all sets in Fig. S14. The shadings indicating the RF_{NC} scenario uncertainty are omitted here for clarity.

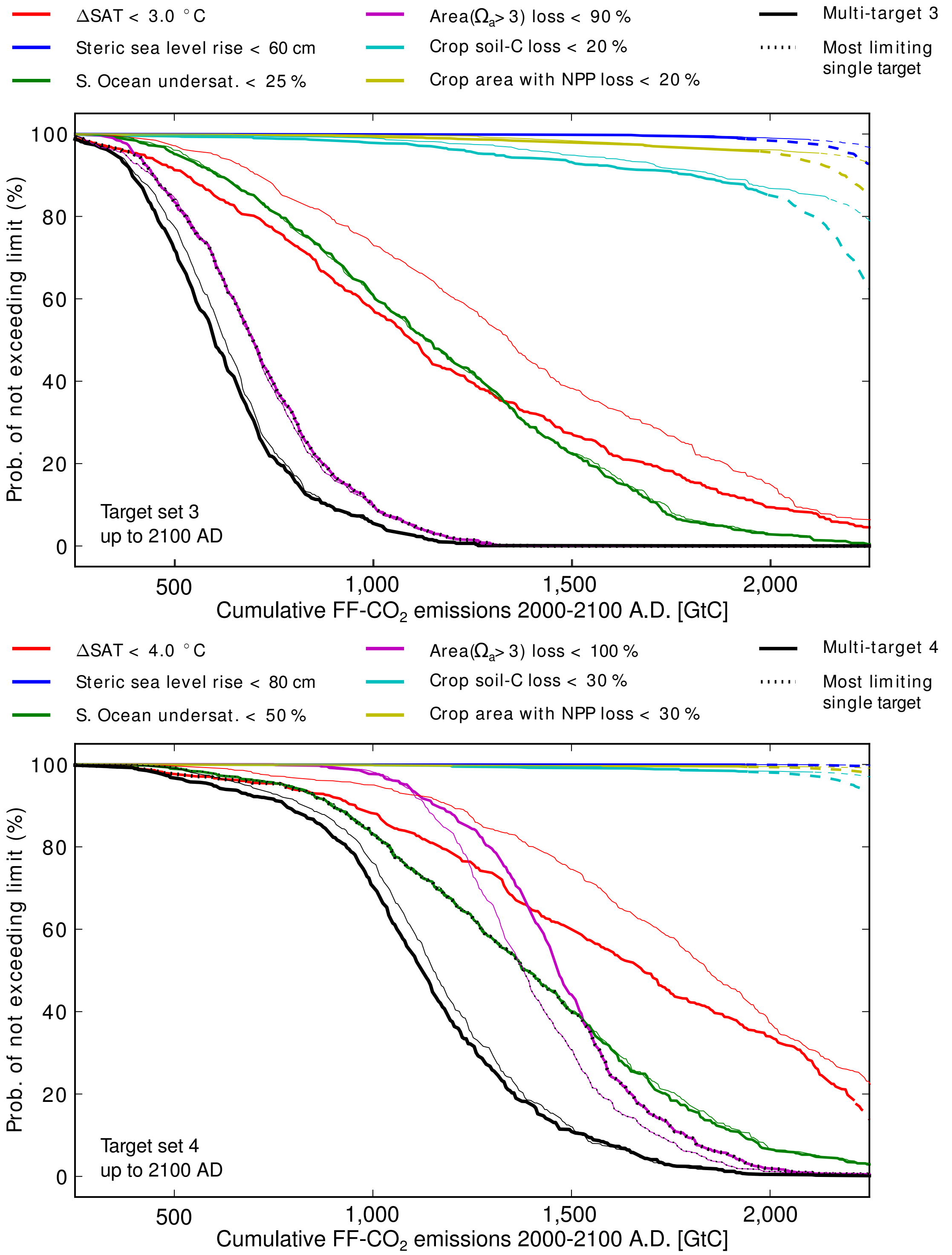

Figure S16: **As Fig. S15, but for the individual targets of set 3 and set 4.**

doi:10.1038/nature12269

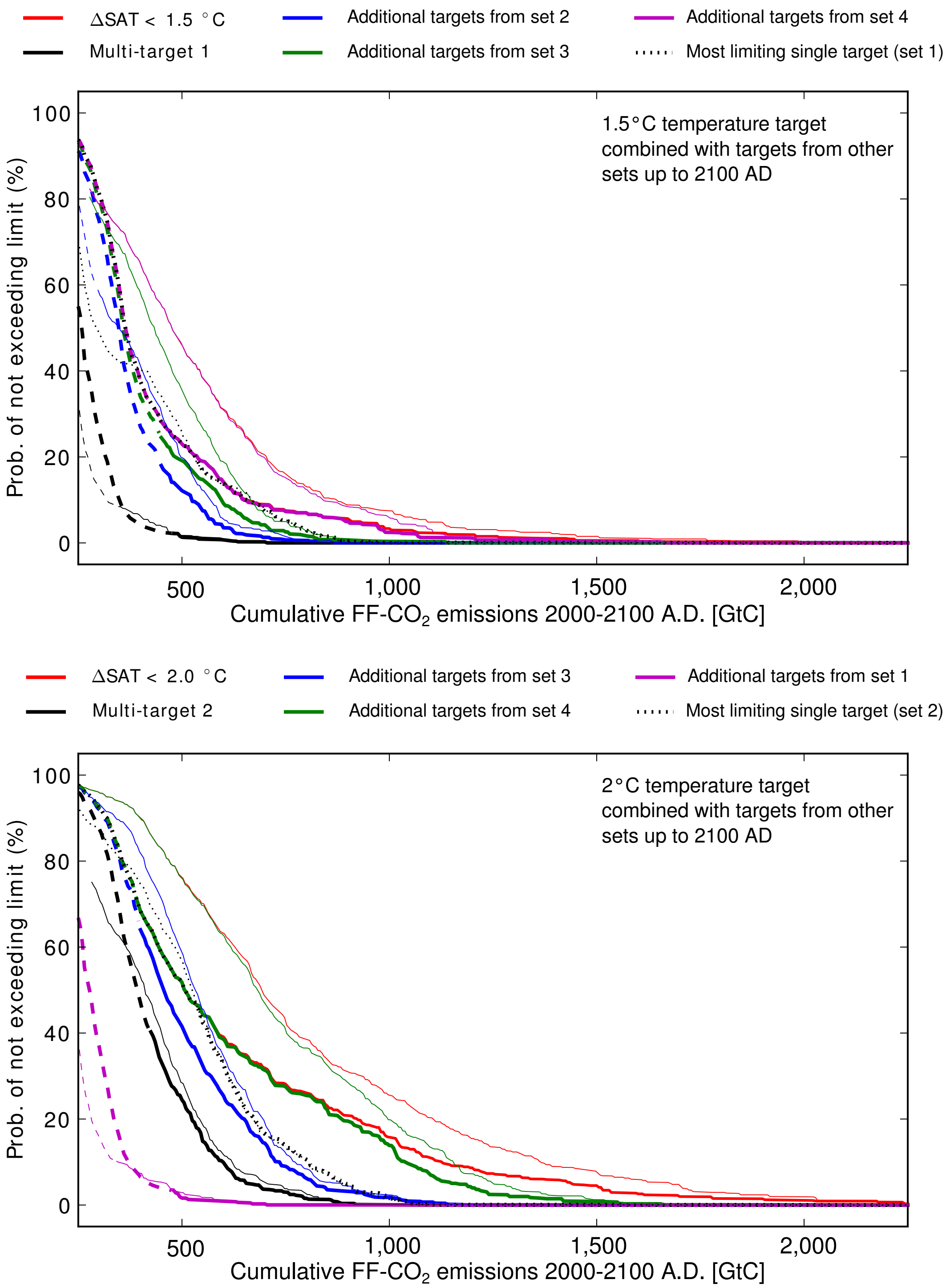

Figure S17: **Sensitivity of the reduction in allowable FF-CO_2 emissions to different combination of targets.** Targets from different sets are applied in addition to the temperature targets 1.5 °C (top) and 2 °C (bottom). The red (temperature target only), black (multi-target), and dotted black (most limiting single target of the set) lines are as shown in Fig. S14. The additional lines (blue, green, magenta) show how the allowable emissions for the multi-target (black) change when the limits from a more/less stringent set are applied for the other five targets variables. Results are given for the RCP, EMF-21 and GGI scenarios (thick lines) and also for all four scenario sets, including the AME scenarios with very low RF_{NC} (thin lines).

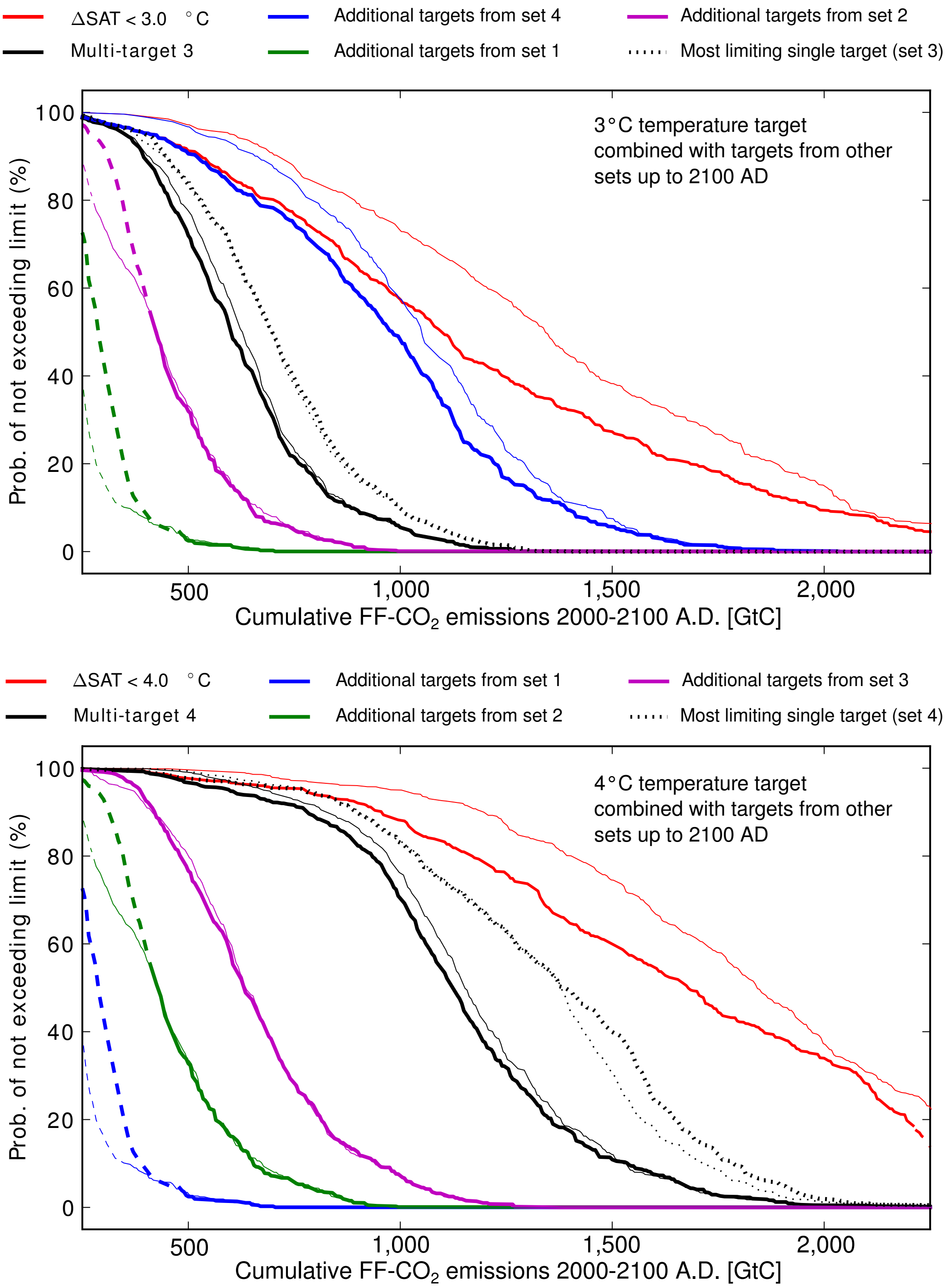

Figure S18: **As Fig. S17, but for the temperature targets 3 °C and 4 °C.**

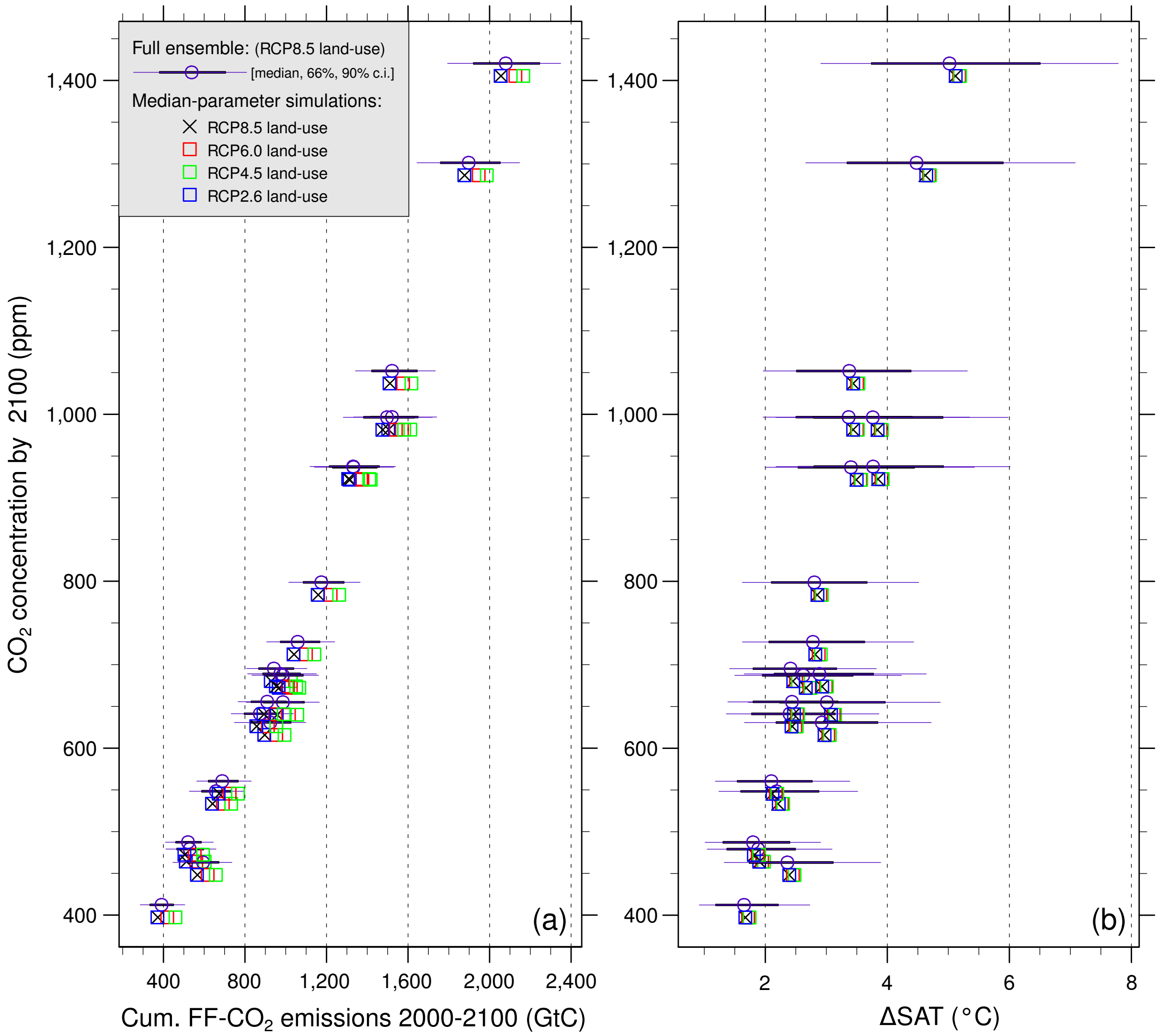

Figure S19: **Sensitivity of results to the choice of the land-use change scenario. (a)** Cumulative 21st century FF-CO_2 emissions and **(b)** ΔSAT for all 22 EMF-21 scenarios. Circles and bars indicate the results from the full ensemble (median, 66%, and 90% confidence intervals) as analyzed in this paper. The crosses and squares below represent additional sensitivity simulations with median parameter settings for each EMF-21 scenario and the four different land-use forcings from the RCPs. The results from the median-parameter simulations are vertically shifted for readability.

Supplementary References

1. Zickfeld, K. *et al.* Long-term climate change commitment and reversibility: An EMIC intercomparison. *J. Climate* (in press, 2013).

2. Eby, M. *et al.* Historical and idealized climate model experiments: an intercomparison of earth system models of intermediate complexity. *Clim. Past* **9**, 1111–1140 (2013). URL `http://www.clim-past.net/9/1111/2013/`.

3. Weaver, A. J. *et al.* Stability of the atlantic meridional overturning circulation: A model intercomparison. *Geophys. Res. Lett.* **39** (2012).

4. Joos, F. *et al.* Carbon dioxide and climate impulse response functions for the computation of greenhouse gas metrics: a multi-model analysis. *Atmos. Chem. Phys.* **13**, 2793–2825 (2013). URL `http://www.atmos-chem-phys.net/13/2793/2013`.

5. Edwards, N. R., Willmott, A. J. & Killworth, P. D. On the role of topography and wind stress on the stability of the thermohaline circulation. *J. Phys. Oceanogr.* **28**, 756–778 (1998).

6. Müller, S. A., Joos, F., Edwards, N. R. & Stocker, T. F. Water mass distribution and ventilation time scales in a cost-efficient, three-dimensional ocean model. *J. Climate* **19**, 5479–5499 (2006).

7. Orr, J. & Najjar, R. G. Abiotic-HOWTO. internal OCMIP report. Tech. rep., LSCE/CEA Saclay, Gif-sur-Yvette, France (1999).

8. Najjar, R. G., Orr, J., Sabine, C. L. & Joos, F. Biotic-HOWTO. internal OCMIP report. Tech. rep., LSCE/CEA Saclay, Gif-sur-Yvette, France (1999).

9. Parekh, P., Joos, F. & Müller, S. A. A modeling assessment of the interplay between aeolian iron fluxes and iron-binding ligands in controlling carbon dioxide fluctuations during antarctic warm events. *Paleoceanography* **23** (2008).

10. Tschumi, T., Joos, F. & Parekh, P. How important are southern hemisphere wind changes for low glacial carbon dioxide? A model study. *Paleoceanography* **23** (2008).

11. Ritz, S. P., Stocker, T. F. & Joos, F. A coupled dynamical ocean-energy balance atmosphere model for paleoclimate studies. *J. Climate* **24**, 349–375 (2011).

12. Ritz, S. P., Stocker, T. F. & Severinghaus, J. P. Noble gases as proxies of mean ocean temperature: sensitivity studies using a climate model of reduced complexity. *Quaternary Sci. Rev.* **30**, 3728–3741 (2011).

13. Berger, A. L. Long-term variations of daily insolation and quaternary climatic changes. *J. Atmos. Sci.* **35**, 2362–2367 (1978).

14. Bintanja, R. The parameterization of shortwave and longwave radiative fluxes for use in zonally averaged climate models. *J. Climate* **9**, 439–454 (1996).

15. Thompson, S. L. & Warren, S. G. Parameterization of outgoing infrared radiation derived from detailed radiative calculations. *J. Atmos. Sci.* **39**, 2667–2680 (1982).

16. Myhre, G., Highwood, E. J., Shine, K. P. & Stordal, F. New estimates of radiative forcing due to well mixed greenhouse gases. *Geophys. Res. Lett.* **25**, 2715–2718 (1998).

17. Joos, F. *et al.* Global warming feedbacks on terrestrial carbon uptake under the Intergovernmental Panel on Climate Change (IPCC) emission scenarios. *Global Biogeochem. Cy.* **15**, 891–907 (2001).

18. Gerber, S. *et al.* Constraining temperature variations over the last millennium by comparing simulated and observed atmospheric CO_2. *Clim. Dynam.* **20**, 281–299 (2003).

19. Sitch, S. *et al.* Evaluation of ecosystem dynamics, plant geography and terrestrial carbon cycling in the LPJ dynamic global vegetation model. *Glob. Change Biol.* **9**, 161–185 (2003).

20. Farquhar, G. D., Caemmerer, S. V. & Berry, J. A. A biochemical-model of photosynthetic CO_2 assimilation in leaves of C-3 species. *Planta* **149**, 78–90 (1980).

21. Strassmann, K. M., Joos, F. & Fischer, G. Simulating effects of land use changes on carbon fluxes: past contributions to atmospheric CO_2 increases and future commitments due to losses of terrestrial sink capacity. *Tellus B* **60**, 583–603 (2008).

22. Stocker, B. D., Strassmann, K. & Joos, F. Sensitivity of Holocene atmospheric CO_2 and the modern carbon budget to early human land use: analyses with a process-based model. *Biogeosciences* **8**, 69–88 (2011).

23. Gerten, D., Schaphoff, S., Haberlandt, U., Lucht, W. & Sitch, S. Terrestrial vegetation and water balance - hydrological evaluation of a dynamic global vegetation model. *J. Hydrol.* **286**, 249–270 (2004).

24. Wania, R., Ross, I. & Prentice, I. C. Integrating peatlands and permafrost into a dynamic global vegetation model: 1. evaluation and sensitivity of physical land surface processes. *Global Biogeochem. Cy.* **23** (2009).

25. Wania, R., Ross, I. & Prentice, I. C. Integrating peatlands and permafrost into a dynamic global vegetation model: 2. evaluation and sensitivity of vegetation and carbon cycle processes. *Global Biogeochem. Cy.* **23** (2009).

26. Spahni, R., Joos, F., Stocker, B. D., Steinacher, M. & Yu, Z. C. Transient simulations of the carbon and nitrogen dynamics in northern peatlands: from the Last Glacial Maximum to the 21st century. *Clim. Past Discuss.* **8**, 5633–5685 (2012).

27. Steinacher, M. *Modeling changes in the global carbon cycle-climate system*. Ph.D. thesis, University of Bern, Bern, Switzerland (2011).

28. Zaehle, S., Sitch, S., Smith, B. & Hatterman, F. Effects of parameter uncertainties on the modeling of terrestrial biosphere dynamics. *Global Biogeochem. Cy.* **19** (2005).

29. Lloyd, J. & Taylor, J. A. On the temperature-dependence of soil respiration. *Funct. Ecol.* **8**, 315–323 (1994).

30. Schmittner, A., Urban, N. M., Keller, K. & Matthews, D. Using tracer observations to reduce the uncertainty of ocean diapycnal mixing and climate-carbon cycle projections. *Global Biogeochem. Cy.* **23** (2009).

31. Müller, S. A., Joos, F., Plattner, G.-K., Edwards, N. R. & Stocker, T. F. Modeled natural and excess radiocarbon: Sensitivities to the gas exchange formulation and ocean transport strength. *Global Biogeochem. Cy.* **22** (2008).

32. Forster, P. *et al. Climate Change 2007: The Physical Science Basis. Contribution of Working Group I to the Fourth Assessment Report of the Intergovernmental Panel on Climate Change*, chap. 2: Changes in Atmospheric Constituents and in Radiative Forcing, 129–234 (Cambridge University Press, Cambridge, United Kingdom and New York, NY, USA, 2007).

33. McKay, M. D., Beckman, R. J. & Conover, W. J. A comparison of three methods for selecting values of input variables in the analysis of output from a computer code. *Technometrics* **21**, 239–245 (1979).

34. Rougier, J. Probabilistic inference for future climate using an ensemble of climate model evaluations. *Clim. Change* **81**, 247–264 (2007).

35. Edwards, N. R., Cameron, D. & Rougier, J. Precalibrating an intermediate complexity climate model. *Clim. Dynam.* **37**, 1469–1482 (2011).

36. Bhat, K. S., Haran, M., Olson, R. & Keller, K. Inferring likelihoods and climate system characteristics from climate models and multiple tracers. *Environmetrics* **23**, 345–362 (2012).

37. Kaminski, T., Heimann, M. & Giering, R. A coarse grid three-dimensional global inverse model of the atmospheric transport - 1. Adjoint model and Jacobian matrix. *J. Geophys. Res.-Atmos.* **104**, 18535–18553 (1999).

38. Masarie, K. A. & Tans, P. P. Extension and integration of atmospheric carbon-dioxide data into a globally consistent measurement record. *J. Geophys. Res.-Atmos.* **100**, 11593–11610 (1995).

39. Moss, R. H. *et al.* The next generation of scenarios for climate change research and assessment. *Nature* **463**, 747–756 (2010).

40. van Vuuren, D. P. *et al.* Representative concentration pathways: an overview. *Clim. Change* (2011).

41. Weyant, J. R., de la Chesnaye, F. C. & Blanford, G. J. Overview of EMF-21: Multigas mitigation and climate policy. *Energ. J.* 1–32 (2006).

42. Van Vuuren, D. P. *et al.* Temperature increase of 21st century mitigation scenarios. *Proc. Nat. Acad. Sci. USA* **105**, 15258–15262 (2008).

43. Grübler, A. *et al.* Integrated assessment of uncertainties in greenhouse gas emissions and their mitigation: Introduction and overview. *Technol. Forecast. Soc.* **74**, 873–886 (2007).

44. Calvin, K. *et al.* The role of asia in mitigating climate change: Results from the asia modeling exercise. *Energ. Econ.* **34, Supplement 3**, S251–S260 (2012).

45. Boden, T., Marland, G. & Andres, B. Global CO_2 emissions from fossil-fuel burning, cement manufacture, and gas flaring: 1751-2008. Data set, Carbon Dioxide Information Analysis Center, Oak Ridge National Laboratory, Oak Ridge, Tennessee 37831-6290, USA (2011). URL `http://cdiac.ornl.gov/ftp/ndp030/global.1751_2009.ems`.

46. Strassmann, K. M., Plattner, G.-K. & Joos, F. CO_2 and non-CO_2 radiative forcings in climate projections for twenty-first century mitigation scenarios. *Clim. Dynam.* **33**, 737–749 (2009).

47. Meinshausen, M. *et al.* The RCP greenhouse gas concentrations and their extension from 1765 to 2300. *Clim. Change* **109**, 213–241 (2011).

48. Taylor, K. E., Stouffer, R. J. & Meehl, G. A. A summary of the CMIP5 experiment design. Tech. Rep., available from http://cmip-pcmdi.llnl.gov/cmip5/experiment_design.html (2009).

49. Hurtt, G. C. *et al.* Harmonization of land-use scenarios for the period 1500-2100: 600 years of global gridded annual land-use transitions, wood harvest, and resulting secondary lands. *Clim. Change* **109**, 117–161 (2011).

50. Crowley et al., T. Volcanism and the Little Ice Age. *PAGES Newsletter* 22–23 (2008).

51. Delaygue, G. & Bard, E. An Antarctic view of Beryllium-10 and solar activity for the past millennium. *Clim. Dynam.* **36**, 2201–2218 (2011).

52. Wang, Y. M., Lean, J. L. & Sheeley, N. R. Modeling the sun's magnetic field and irradiance since 1713. *Astrophys. J.* **625**, 522–538 (2005).

53. Bullister, J. Atmospheric CFC-11, CFC-12, CFC-113, CCl_4 and SF_6 histories. Data set, Carbon Dioxide Information Analysis Center, Oak Ridge National Laboratory, US Department of Energy, Oak Ridge, Tennessee (2011). URL http://cdiac.ornl.gov/ftp/oceans/CFC_ATM_Hist/.

54. McCormac, F. G. *et al.* SHCal04 Southern Hemisphere calibration, 0–11.0 cal kyr BP. *Radiocarbon* **46**, 1087–1092 (2004).

55. Reimer, P. J. *et al.* IntCal09 and Marine09 radiocarbon age calibration curves, 0–50,000 years cal BP. *Radiocarbon* **51**, 1111–1150 (2009).

56. Orr, J. C. On ocean carbon-cycle model comparison. *Tellus B* **51**, 509–510 (1999).

57. Isaaks, E. H. & Srivastava, R. M. *Applied Geostatistics*, chap. 12: Ordinary Kriging, 278–322 (Oxford University Press, New York, USA, 1989).

58. Haxeltine, A. & Prentice, I. C. A general model for the light-use efficiency of primary production. *Funct. Ecol.* **10**, 551–561 (1996).

59. Hallgren, W. S. & Pitman, A. J. The uncertainty in simulations by a global biome model (BIOMES) to alternative parameter values. *Glob. Change Biol.* **6**, 483–495 (2000).

60. Collaty, G. J., Berry, J. A., Farquhar, G. D. & Pierce, J. The relationship between the rubisco reaction-mechanism and models of photosynthesis. *Phys. Chem. Earth* **13**, 219–225 (1990).

61. Leverenz, J. W. The effects of illumination sequence, CO_2 concentration, temperature and acclimation on the convexity of the photosynthetic light response curve. *Physiol. Plantarum* **74**, 332–341 (1988).

62. Magnani, F., Leonardi, S., Tognetti, R., Grace, J. & Borghetti, M. Modelling the surface conductance of a broad-leaf canopy: effects of partial decoupling from the atmosphere. *Phys. Chem. Earth* **21**, 867–879 (1998).

63. Bartelink, H. H. A model of dry matter partitioning in trees. *Tree Physiol.* **18**, 91–101 (1998).

64. Raich, J. W. & Schlesinger, W. H. The global carnon-dioxide flux in soil respiration and its relationship to vegetation and climate. *Tellus B* **44**, 81–99 (1992).

65. Trumbore, S. E. Age of soil organic matter and soil respiration: radiocarbon constraints on belowground C dynamics. *Ecol. Appl.* **10**, 399–411 (2000).

66. Jenkinson, D. S. The turnover of organic-carbon and nitrogen in soil. *Philos. T. Roy. Soc. B* **329**, 361–368 (1990).

67. Kergoat, L. A model for hydrological equilibrium of leaf area index on a global scale. *J. Hydrol.* **212**, 268–286 (1998).

68. Tarnocai, C. *et al.* Soil organic carbon pools in the northern circumpolar permafrost region. *Global Biogeochem. Cy.* **23** (2009).

69. Knutti, R., Stocker, T. F., Joos, F. & Plattner, G. K. Probabilistic climate change projections using neural networks. *Clim. Dynam.* **21**, 257–272 (2003).

70. Meinshausen, M. *et al.* Greenhouse-gas emission targets for limiting global warming to 2 °C. *Nature* **458**, 1158–1162 (2009).

71. Edwards, N. & Marsh, R. Uncertainties due to transport-parameter sensitivity in an efficient 3-D ocean-climate model. *Clim. Dynam.* **24**, 415–433 (2005).

72. Huang, B. Y., Stone, P. H., Sokolov, A. P. & Kamenkovich, I. V. Ocean heat uptake in transient climate change: Mechanisms and uncertainty due to subgrid-scale eddy mixing. *J. Climate* **16**, 3344–3356 (2003).

73. GLOBALVIEW-CO2. Cooperative atmospheric data integration project - carbon dioxide. CD-ROM, NOAA ESRL, Boulder, Colorado (2011). Also available on Internet via anonymous FTP to ftp.cmdl.noaa.gov, Path: ccg/co2/GLOBALVIEW.

74. Gobron, N. *et al.* Evaluation of fraction of absorbed photosynthetically active radiation products for different canopy radiation transfer regimes: Methodology and results using Joint Research Center products derived from SeaWiFS against ground-based estimations. *J. Geophys. Res.-Atmos.* **111** (2006).

75. NPP multi-biome: NPP and driver data for ecosystem model-data intercomparison. Data set, Oak Ridge National Laboratory Distributed Active Archive Center, Oak Ridge, Tennessee, U.S.A. (2001). URL `http://www.daac.ornl.gov`.

76. Luyssaert, S. *et al.* CO_2 balance of boreal, temperate, and tropical forests derived from a global database. *Glob. Change Biol.* **13**, 2509–2537 (2007).

77. Global Soil Data Task Group. Global gridded surfaces of selected soil characteristics (IGBP-DIS). Data set doi:10.3334/ORNLDAAC/569, Oak Ridge National Laboratory Distributed Active Archive Center, Oak Ridge, Tennessee, U.S.A. (2000). URL `http://www.daac.ornl.gov`.

78. Tarnocai, C., Swanson, D., Kimble, J. & Broll, G. Northern circumpolar soil carbon database. Digital Database, Research Branch, Agriculture and Agri-Food Canada, Ottawa, Canada (2007). URL `http://wms1.agr.gc.ca/NortherCircumpolar/northercircumpolar.zip`.

79. Batjes, N. H. Total carbon and nitrogen in the soils of the world. *Eur. J. Soil Sci.* **47**, 151–163 (1996).

80. Keith, H., Mackey, B. G. & Lindenmayer, D. B. Re-evaluation of forest biomass carbon stocks and lessons from the world's most carbon-dense forests. *Proc. Nat. Acad. Sci. USA* **106**, 11635–11640 (2009).

81. Prentice, I. C. *et al.* *Climate Change 2001: The Scientific Basis. Contribution of Working Group I to the Third Assessment Report of the Intergovernmental Panel on Climate Change*, chap. The Carbon Cycle and Atmospheric Carbon Dioxide, 183–237 (Cambridge University Press, Cambridge, United Kingdom and New York, NY, USA, 2001).

82. Locarnini, R. A. *et al.* World ocean atlas 2009, volume 1: Temperature. NOAA Atlas NESDIS 68, U.S. Government Printing Office, Washington, D.C. (2010).

83. Antonov, J. I. *et al.* World ocean atlas 2009, volume 2: Salinity. NOAA Atlas NESDIS 69, U.S. Government Printing Office, Washington, D.C. (2010).

84. Garcia, H. E. *et al.* World ocean atlas 2009, volume 4: Nutrients (phosphate, nitrate, silicate). NOAA Atlas NESDIS 71, U.S. Government Printing Office, Washington, D.C. (2010).

85. Key, R. M. *et al.* A global ocean carbon climatology: Results from Global Data Analysis Project (GLODAP). *Global Biogeochem. Cy.* **18** (2004).

86. Etheridge, D. M. *et al.* Natural and anthropogenic changes in atmospheric CO_2 over the last 1000 years from air in antarctic ice and firn. *J. Geophys. Res.-Atmos.* **101**, 4115–4128 (1996).

87. Keeling, C. D. & Whorf, T. P. *Atmospheric CO_2 records from sites in the SIO air sampling network*. Trends Online: A compendium of Data on Global Change (Carbon Dioxide Information Analysis Center, Oak Ridge National Laboratory, US Department of Energy, Oak Ridge, Tenn., U.S.A., 2005).

88. Conway, T. & Tans, P. Trends in atmospheric carbon dioxide. Data set, NOAA/ESRL (2011). Available on-line: http://www.esrl.noaa.gov/gmd/ccgg/trends/.

89. Canadell, J. G. *et al.* Contributions to accelerating atmospheric CO_2 growth from economic activity, carbon intensity, and efficiency of natural sinks. *Proc. Nat. Acad. Sci. USA* **104**, 18866–18870 (2007).

90. Brohan, P., Kennedy, J. J., Harris, I., Tett, S. F. B. & Jones, P. D. Uncertainty estimates in regional and global observed temperature changes: A new data set from 1850. *J. Geophys. Res.-Atmos.* **111** (2006).

91. Levitus, S. *et al.* World ocean heat content and thermosteric sea level change (0-2000 m), 1955-2010. *Geophys. Res. Lett.* **39** (2012).

92. Lyman, J. M. *et al.* Robust warming of the global upper ocean. *Nature* **465**, 334–337 (2010).

93. von Schuckmann, K. & Le Traon, P.-Y. How well can we derive global ocean indicators from Argo data? *Ocean Sci.* **7**, 783–791 (2011).

94. Zickfeld, K., Eby, M., Matthews, H. D. & Weaver, A. J. Setting cumulative emissions targets to reduce the risk of dangerous climate change. *Proc. Nat. Acad. Sci. USA* **106**, 16129–16134 (2009).

95. Rogelj, J., Meinshausen, M. & Knutti, R. Global warming under old and new scenarios using IPCC climate sensitivity range estimates. *Nat. Clim. Ch.* **2**, 248–253 (2012).

96. Meehl, G. A. *et al.* Relative outcomes of climate change mitigation related to global temperature versus sea-level rise. *Nat. Clim. Ch.* **2**, 576–580 (2012).

97. Boden, T. & Andres, B. Global CO_2 emissions from fossil-fuel burning, cement manufacture, and gas flaring: 1751-2009. Data set, Carbon Dioxide Information Analysis Center, Oak Ridge National Laboratory, Oak Ridge, Tennessee 37831-6290, USA (2012). URL `http://cdiac.ornl.gov/trends/emis/meth_reg.html`.